Eur. Phys. J. A **11**, 467–490 (2001)

THE EUROPEAN PHYSICAL JOURNAL A

Spallation neutron production and the current intra-nuclear cascade and transport codes

D. Filges[1], F. Goldenbaum[1,a], M. Enke[2], J. Galin[3], C.-M. Herbach[2], D. Hilscher[2], U. Jahnke[2], A. Letourneau[3], B. Lott[3], R.-D. Neef[1], K. Nünighoff[1], N. Paul[1], A. Péghaire[3], L. Pienkowski[4], H. Schaal[1], U. Schröder[5], G. Sterzenbach[1], A. Tietze[6], V. Tishchenko[2,b], J. Toke[5], and M. Wohlmuther[1]

[1] Forschungszentrum Jülich GmbH, Institut für Kernphysik, D-52425 Jülich, Germany
[2] Hahn-Meitner Institut Berlin GmbH, Glienickerstr.100, D-14109 Berlin, Germany
[3] GANIL, BP 5027, F-14076 Caen Cedex 5, France
[4] Heavy Ion Laboratory Warsaw University, Pasteura 5a, 02-093 Warszawa, Poland
[5] University of Rochester, Rochester, New York 14627, USA
[6] Universität Wuppertal, 42329 Wuppertal, Germany

Received: 22 May 2001 / Revised version: 31 August 2001
Communicated by W. Henning

Abstract. A recent renascent interest in energetic proton-induced production of neutrons originates largely from the inception of projects for target stations of intense spallation neutron sources, like the planned European Spallation Source (ESS), accelerator-driven nuclear reactors, nuclear waste transmutation, and also from the application for radioactive beams. In the framework of such a neutron production, of major importance is the search for ways for the most efficient conversion of the primary beam energy into neutron production. Although the issue has been quite successfully addressed experimentally by varying the incident proton energy for various target materials and by covering a huge collection of different target geometries —providing an exhaustive matrix of benchmark data— the ultimate challenge is to increase the predictive power of transport codes currently on the market. To scrutinize these codes, calculations of reaction cross-sections, hadronic interaction lengths, average neutron multiplicities, neutron multiplicity and energy distributions, and the development of hadronic showers are confronted with recent experimental data of the NESSI collaboration. Program packages like HERMES, LCS or MCNPX master the prevision of reaction cross-sections, hadronic interaction lengths, averaged neutron multiplicities and neutron multiplicity distributions in thick and thin targets for a wide spectrum of incident proton energies, geometrical shapes and materials of the target generally within less than 10% deviation, while production cross-section measurements for light charged particles on thin targets point out that appreciable distinctions exist within these models.

PACS. 25.40.Sc Spallation reactions – 24.10.Lx Monte Carlo simulations (including hadron and parton cascades and string breaking models) – 28.20.-v Neutron physics

1 Introduction

Neutron production in spallation reactions induced by energetic particles in heavy targets has been observed already in the late 40's. As a result of a continuous progress in accelerator technology, the construction of powerful spallation sources has now become possible, providing new opportunities for solid state physics, life and material science. In fact, a variety of projects have been initiated recently, including the construction at the Paul Scherer Institute (SINQ) [1] of an accelerator-based, continuous neutron source and including several pulsed, high-intensity neutron sources, planned or under construction. Among the latter projects are the 5 MW European Spallation Source [2], a 2 MW Spallation Neutron Source [3,4] in the US, and the Japanese facility at JAERI/KEK [5].

Intense, short-pulse neutron beams from accelerator-based sources make it possible to study a wide range of scientific problems via neutron scattering, exploiting time-of-flight techniques and allowing kinetic studies of various processes. In addition, powerful neutron sources, such as the subcritical spallation/fission hybrids [6,7], provide a basis for various, potentially important applications. For example, such facilities may be used to effectively produce tritium [8] or to achieve the incineration or transmutation

[a] e-mail: f.goldenbaum@fz-juelich.de
[b] On leave from Flerov Laboratory of Nuclear Reactions, JINR, 141980 Dubna, Joliot-Curie 6, Russia.

of radioactive nuclear waste [9]. It is also important that the accelerator-based neutron sources are much more acceptable from the environmental point of view than nuclear reactors and that they show greater promise for future improvements in peak neutron intensities.

Systematics of neutron production cross-sections and neutron energy spectra as a function of incident proton energy, target material, and target geometry is not well known or documented in the literature. In order to fill these gaps in the systematics, the NESSI (Neutron Scintillator and Silicon Detector), as well as the former PS208 collaboration at CERN, have performed a series of experiments [10–13] using a highly efficient 4π gadolinium-loaded scintillator detector [14]. These measurements covered a large range of incident proton energies, as well as a variety of target materials and geometries. In contrast to the older investigations on *average* neutron multiplicities [15–19], the NESSI experiments have provided also *event-by-event* information.

The extensive set of benchmark data obtained in the NESSI experiments imposes strong constraints on the theoretical modeling of the occurring interactions [20], and allows one to calibrate and improve widely used high-energy transport codes. The accuracy of such codes is critical for the design of high-power target stations, since the optimization of geometrically expendable high-power target stations will finally rely on general Monte Carlo particle transport codes having maximum predictive power.

H and He production cross-sections have been measured by the NESSI collaboration [21,22] and experimental excitation energy distributions have been deduced — following a procedure described in ref. [23]. Unfortunately the experimental setup of NESSI [10,21] is not suited for measuring the kinetic energy or angular distributions of neutrons. Energy spectra and angular distributions of neutrons have recently been measured [24–28]. Isotopic distributions and kinetic energies of residual nuclides, which induce radiation damage in target and structure materials, have been studied at GSI [29–32]. These additional observables certainly are of large interest for representing even more constraints to the models, but will not be the major task here.

The present paper focuses on a comparison of the theoretical predictions obtained with different program packages, such as HERMES [33,34], LCS2.70 [35], or MCNPX2.1.5 [36]. In addition to the above Intra-Nuclear Cascade (INC) codes, derivatives of the Bertini code [37], the present study uses also the time-dependent Liege INCL2.0 code [38,39]. Essential features of these codes are described briefly in sect. 2. The choice of the model parameters used in the present simulation calculations is discussed separately in sect. 3.

In the case of thick targets, the overall reaction scenario includes secondary and higher-order reactions induced by the reaction products themselves and, therefore, the calculations must include a 3-dimensional simulation of inter-nuclear cascades. Such a 3-dimensional description of the propagation of the inter-nuclear cascade and the transport of particles in thick targets is a rather complex problem that involves dealing with various boundary conditions. This issue is addressed in sect. 4, where the propagation of various species of particle types (p, n) is considered separately in longitudinal and radial directions.

After a brief description of the NESSI setup in sect. 5, sect. 6 is dedicated to comparing the results of simulation calculations to the experimental data. Such a comparison has revealed serious limitations of the mainstream models. Some striking deficiencies of the theoretical models are then discussed separately in sect. 7.

2 Modeling of transport processes

An energetic particle entering a massive target gives rise to a complex chain of interactions resulting in the emission of various particles, some of which are able to escape the target volume. The latter particles can be detected in the experiment and provide information on the transport processes involved. As mentioned previously, these processes can be viewed as a convolution of two types of cascades, such that particles released in a primary Intra-Nuclear Cascade [40] (INC) give rise to an inter-nuclear cascade of secondary and higher-order reactions in the surrounding target material. Therefore, interpretation of the experimental data in terms of physical processes requires proper modeling of the convolution of these two types of cascades and of the detector response.

In the present study, two sets of computer programs are considered, which generate predictions that can be compared to the experimental observations. These sets are the High-Energy Radiation Monte Carlo Elaborate System (HERMES) [33,34] package and the Los Alamos High-Energy Transport (LAHET) Code System (LCS) [35]. Both sets of programs model the multibody problem numerically [37–39,41] using Monte Carlo techniques. They both use within their INC part the following simplifying assumptions:

- The hadron-nucleus interaction is a sequence of independent collisions of primary and secondary particles with the nucleons of the nucleus.
- The cascade particles follow classical trajectories and do not interact with each other.
- The interaction is based on free elementary cross-sections. In-medium effects are generally not taken into account. These cross-sections have been derived from empirical approximations of

$$\begin{aligned}
\pi N &\rightarrow \pi N \quad \text{(elastic)},\\
NN &\rightarrow NN \quad \text{(elastic)},\\
NN &\rightarrow N^*N \rightarrow N\pi N,\\
NN &\rightarrow N^*N^* \rightarrow N\pi N\pi,\\
\pi N &\rightarrow \pi N^* \rightarrow \pi N\pi,\\
N^*N &\rightarrow NN \quad \text{(delta absorption)},\\
\pi N &\rightarrow \pi N \quad \text{(charge exchange)}
\end{aligned}$$

data; Pauli blocking, the Fermi motion of the target and projectile nuclei, pion production, and the effects of the target mean field are included.

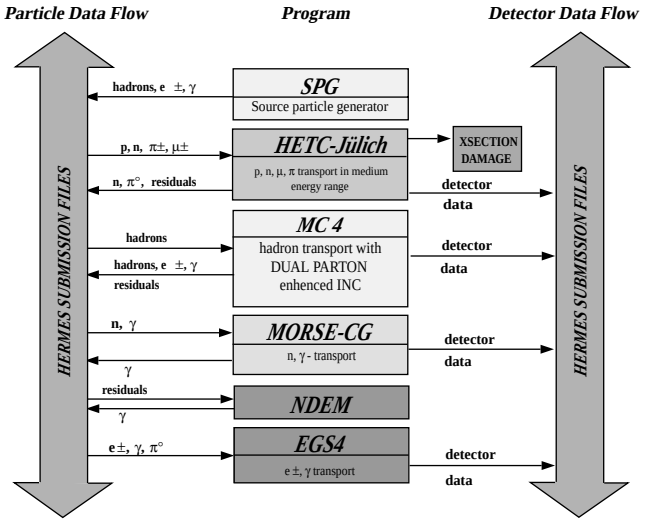

Fig. 1. The HERMES processing diagram.

– The nucleus is viewed as degenerate Fermi gas of neutrons and protons.

The assumptions for which the fundamental presumptions (within the INC) are valid are:

1. the De Broglie wavelength λ of cascade particles is smaller than the average distance of nucleons in the nucleus ($\delta \approx 1.3\,\mathrm{fm}$) and the mean free path length L in nuclear matter: $\lambda \ll \delta, \lambda \ll L$;
2. the duration of the elementary impact $\tau_{\mathrm{int}} \sim r_{\mathrm{int}}/v$ is smaller than the time between two collisions, *i.e.* the radius of strong interaction is smaller than the mean free path length: $r_{\mathrm{int}} \ll L$;
3. the number of participating cascade particles N_{c} should be considerably smaller than the number of target nucleons $A_{\mathrm{t}} : N_{\mathrm{c}} \ll A_{\mathrm{t}}$.

HERMES [33,34] is a collection of Monte Carlo codes simulating the transport of particles through and the interaction with matter. The process diagram of the HERMES package is presented in fig. 1. There are six constituent computer codes in the HERMES package describing the projectile production (SPG), the interactions induced in the target material by various classes of particles in various energy ranges (HETC-Jülich, MC4, MORSE-CG, EGS4), as well as the de-excitation of target residues (NDEM). These constituent computer codes exchange input/output data via standardized HERMES submission files, such that a particle or a γ-ray data found in the output of one program is used as an input for the program that is best suited for its handling. Then this particular program takes on itself to follow the subsequent history of the particle in question.

Within the HERMES package (fig. 1), the hadronic part of the particle shower is modeled by the High-Energy Transport Code HETC-Jülich or alternatively the Monte Carlo code MC4 [33] both comprising the fission/evaporation process. In brief, MC4 is the successor package of HERMES and will be publicly available in the near future. Low-energy neutrons ($E \leq 20$ MeV) are handled by the code MORSE [34,42] utilizing the Evaluated Nuclear Data File/B (ENDF/B)-based neutron cross-section libraries. The de-excitation of residues by γ-emission is handled by the Nucleus De-Excitation Module NDEM. The history of the γ-rays resulting from the latter decay, as well as of those originating from the π^0 decay, is then followed by the Electron Gamma Shower code EGS4 [43]. A suite of additional programs was used to perform simple data management and analysis functions.

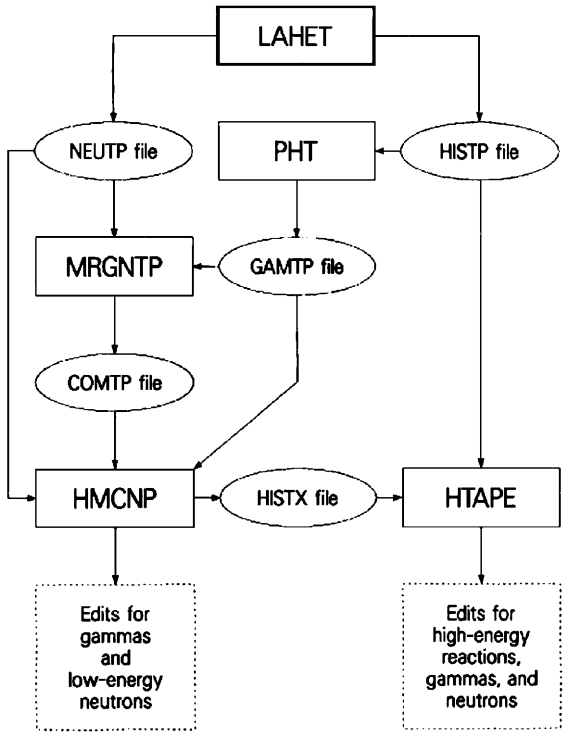

Fig. 2. LCS and data files (cf. ref. [35]).

The HERMES package allows one to model the history of secondary particles produced in primary collisions at energies ranging from thermal to relativistic. It considers explicitly protons, neutrons, $\pi^{\pm}, \pi^0, \mu^{\pm}, e^{\pm}$, and light ions up to a mass number of $A = 10$, and allows one to treat complex geometries and material configurations.

The structure of the Los Alamos High-Energy Transport Code System (LCS) [35] is illustrated in fig. 2. In this case, the hadronic part of the particle shower is modeled by the Los Alamos High-Energy Transport code LAHET, while particle tracking is handled by the LANL Monte Carlo N-Particle (MCNP) code [44]. The code PHT is used to generate from the LAHET output file a photon source file, which is then used as input for the code HMCNP. The latter is a derivative of the MCNP code, now accepting external neutron and photon data files created by LAHET or PHT. The file generated by PHT includes data on pions and de-excitation γ-rays. Information on neutrons of energies below 20 MeV is written to a source file for further processing with HMCNP. HTAPE is a general-purpose sorting routine for LAHET history files. Simulation observables include surface current and flux, neutron

Table 1. Set of standard parameters for HERMES, LCS and MCNPX. Details are given in refs. [34–36,47,48,50].

Basic assumptions	
Intra-nuclear cascade	Bertini INC
Monte Carlo technique	"space-like"
Nuclear density distribution	$\rho(r) = \rho_0(\exp((r-c)/a)+1)^{-1}$; $c = 1.07A^{1/3}$ fm, $a = 0.545$ fm, $\rho_0 = 0.17Ze/A$ fm^{-3}, $\rho(r) = \alpha_i\rho_0$, $\alpha_1 = 0.9$, $\alpha_2 = 0.2$, $\alpha_3 = 0.01$
Nuclear density depletion	not considered
Options which may be chosen by the user	
Cutoff energy for switching INC/evaporation	7 MeV (n), 7 MeV + Coulomb barrier (p)
Equilibrium stage	Dresner model [50] for n, p, d, t, ^{3}He, ^{4}He emission + fission + γ
Fission-evaporation model	RAL [47,48]
Level density description	HETC (cf. subsect. 3.1)
B_0 parameters	Pb: $a = A/10$, W, Hg: $a = A/8$
Coulomb barriers	according to eq. (4)
Elastic scattering	switched on for protons, neutrons
Cutoff energy for n transport	HETC $E^n_{\rm kin} > 20$ MeV, MORSE/MCNP $E^n_{\rm kin} \leq 20$ MeV
Cutoff energy for p, π, μ transport	1, 0.149 and 0.113 MeV (only HETC)
Proton beam	pencil beam
Pre-equilibrium model	off

track length flux, particle yields and energy spectra, energy deposits and balance, distribution of residual nuclei and their excitation energies.

LAHET code offers two options for handling intra-nuclear cascades. As an alternative to the Bertini [37] intra-nuclear cascade code used in HERMES, it includes the ISABEL [45,46] INC routines, which allow one to treat also nucleus-nucleus interactions. In the ISABEL INC routines, the nuclear density is approximated by up to 16 discrete bins, rather than by three bins as in the Bertini INC code.

In modeling the de-excitation of the produced excited nuclei due to fission/evaporation, the HERMES package relies on the RAL [47,48] code. LAHET includes additionally the ORNL [49] description which is restricted to fission for elements with $Z \geq 91$. Both statistical evaporation models are implemented in the Dresner evaporation code [50,51] based on the Weisskopf-Ewing approach. The disintegration of light nuclei ($A \leq 20$) can be modeled optionally by the Fermi breakup model [52]. Baryon number, charge, energy and momentum are conserved in all codes.

Within the two packages, the switching from a code modeling a fast INC process to one modeling the subsequent disintegration of the nucleus by statistical evaporation processes is generally controlled by particle energy values. The switch occurs whenever the kinetic energy of the fastest cascade particle inside the target nucleus is not sufficient to overcome the energy neccessary to escape from the nucleus. In LCS, the value of the neutron cutoff energy is randomly chosen between zero and twice the mean binding energy. For protons, this code assumes a cutoff energy that is equal to the larger of the two, the Coulomb barrier or the neutron cutoff energy. HERMES, on the other hand, uses for the cutoff energies fixed values of 7 MeV and 7 MeV plus the Coulomb barrier, for neutrons and protons, respectively.

The LCS provides an option of including, as an intermediate step between the fast INC and the slow evaporation process, pre-equilibrium processes. The latter are modeled by the multistage exciton model (MPM) [53] and allow one to handle the formation of composite particles like deuterons, tritons, ^{3}He and α-particles (beyond the emission of neutrons and protons) *before* statistical equilibrium is reached.

Particles are transported until a lower energy threshold of $E_{\rm min}$ is reached. Values of this threshold are set to 1 MeV, 0.149 MeV, and 0.113 MeV, for protons, pions, and muons, respectively.

Unless stated otherwise in specific cases, in most simulation calculations discussed in the following sections, the set of standard parameters listed in table 1 was used. The various codes packages differ essentially by the choice of the parameters (cf. sect. 3), improvements implemented in the original models or because they include alternative specifications or prescriptions.

3 Parameter discussion

In fact from the simulation point of view there is a great variety of models, parameters and options implemented in all program suites under consideration in the current contribution that can be used to describe the physical behavior of a system.

A multitude of different INC models (Bertini, ISABEL, INCL2.0 and many more) is applicable and many parameters not only within the INC codes, but also within the statistical evaporation codes appended, may influence the resulting abundance or spectra of particles created.

LCS offers a great freedom in the choice of different level density descriptions, *e.g*, the Gilbert-Cameron-Cook-Ignatyuk, the HETC, and the Jülich model. As mentioned optionally the Multistage Pre-Equilibrium Model (MPM) [53] can be switched between INC and the equilibrium phase.

Different descriptions of Coulomb barriers in the RAL [47,48] and Dresner models [50,51] are resulting in rather different production cross-sections particular for charged particles (but also for neutrons). The models assume constant or excitation energy-dependent Coulomb barriers.

Therefore, a study was performed in order to investigate the predictive power of the combination of these models by intercomparing theoretical models and confronting the various approaches with experimental results. In the following, first a fragmentary assortment of biasing aspects will be given. We do not raise the claim to exhaust the limitless diversity of parameters offered by all program suites.

3.1 Level density description

The parameter affecting the decay width Γ of particles emitted during the evaporation process is the level density parameter a. One option to describe a is the energy-independent HETC formalism. In this case parameterization is done via the B_0 parameter [34,54] and the level density is given by

$$a = \frac{A}{B_0} \cdot \left(1 + \frac{Y\Delta^2}{A^2}\right), \tag{1}$$

with A the mass number, $\Delta = A - 2Z$, Z the charge number and Y being a value normally set to 1.5. In this contribution for all incident proton energies the level density parameters B_0 have been chosen conventionally to be 8 MeV^{-1} for W and Hg and 10 MeV^{-1} for Pb due to shell effects for the latter nucleus. However, this choice might not be fully justified for the Pb target taking into account that most of the nuclei at the end of the cascades are removed from Pb and moreover, excited enough for the shell effects to be, at least, partially washed out.

Another model provided by LCS includes excitation energy damped shell effects of the level densities by using the Ignatyuk formalism [55] as implemented in the GNASH code [56]. The level density parameter a is calculated via

$$a(E^*) = \alpha \left[1 + \left(\frac{\left(1 - e^{-\gamma E^*}\right)\delta W}{E^*}\right)\right], \tag{2}$$

where α is the asymptotic value of $\lim_{E^* \to \infty} a(E^*)$ given as a function of mass, $\gamma = 0.05$ MeV^{-1}, and δW is a term concerning shell effects. Another provision is that $\lim_{E^* \to 0} a(E^*) = a_0$, with a_0 being the Gilbert-Cameron-Cook-Ignatyuk (GCCI) level density parameterization [57].

The third possibility of parameterization is the Jülich level density formulation. This model is using energy-independent B_0 parameters tabulated as a function of mass [34].

In the calculations performed, the HETC and the GCCI level density descriptions have been applied. Calculations with the Jülich level density model have not been executed, because this model is only valid in the low excitation energy domain where shell effects act.

3.2 Coulomb barriers for charged particle emission and feedback on neutrons

The excited compound nuclei (mass A), atomic number Z, and thermal excitation energy E^* formed after the INC are de-exciting by the emission of various particles, *e.g.* neutrons, protons, deuterons, etc.

Within the models, there are different descriptions of the effective barriers, to which —in contrast to neutrons— charged particles are subject during their evaporation.

The HERMES or LCS/MCNPX program packages have the possibility to select optionally between the ORNL/Dresner description [50] and the RAL [47,48] formalism.

The effective barriers V_x in the Dresner formalism read

$$V_x = 0.846927 \cdot k_x \cdot \frac{Z_{\mathrm{ejec}} \cdot Z}{R_x + R}, \tag{3}$$

whereby Z_{ejec} and Z are the atomic numbers and R_x and R the atomic radii of the ejectile (tabulated) and destination nucleus $R = (A - A_{\mathrm{ejec}})^{1/3}$, respectively. The tabulated factors $k_x \leq 1$ for different Z_{ejec} of ejectiles make allowance for a potential barrier penetration.

The description in the RAL formalism, following the Le Couteur approach [58], is very similar to the ORNL/Dresner description (cf. eq. (5)), except that the Coulomb barriers are further down-scaled by a factor [59]

$$V_x = V_x \cdot \left(1 + 0.005 \cdot \frac{E^*}{Z_{\mathrm{ejec}}}\right)^{-1}, \tag{4}$$

with E^* being the thermal excitation energy of the evaporating nucleus. The original idea of the Coulomb reduction was to take account for an E^*-dependent shape deformation during the emission like the one well established for the fission process. The exact relation between the ORNL/Dresner and the RAL Coulomb barriers for $E^* = 0$ MeV is:

$$V_{\mathrm{C}}(\mathrm{ORNL}) = 1.042 \cdot V_{\mathrm{C}}(\mathrm{RAL}, E^* = 0) \tag{5}$$

In the statistical evaporation code GEMINI [60] —optionally chosen for the calculations of production

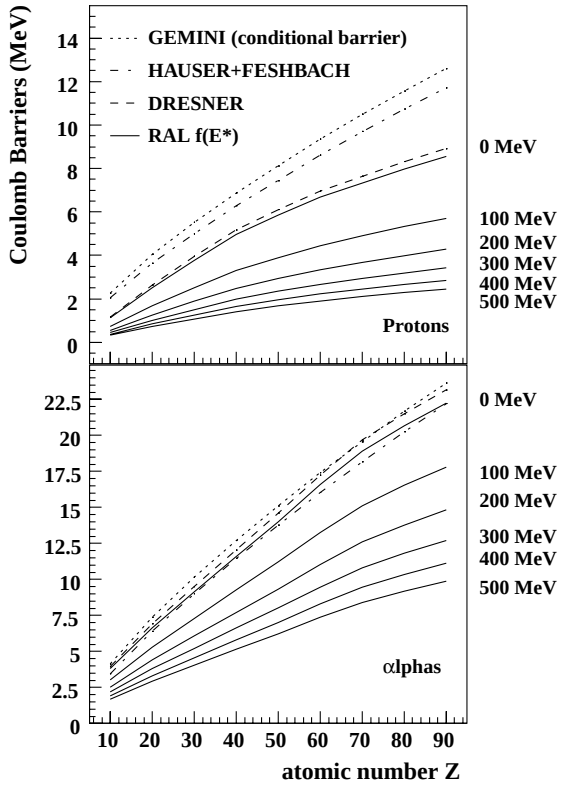

Fig. 3. Coulomb barriers as a function of Z of the emitting compound nucleus for protons (top) and α-particles (bottom) following various models. For the RAL option (solid lines) the influence of the thermal excitation energy on the Coulomb barrier is indicated on the right-hand side.

cross-sections in subsect. 6.3— the Coulomb barrier is given by

$$V_x = \frac{1.44 \cdot Z_{\mathrm{ejec}} \cdot Z}{r_0 \cdot (A_{\mathrm{ejec}}^{1/3} + A^{1/3}) + s}\,, \qquad (6)$$

with $s = 2\,\mathrm{fm}$ and the nuclear radius parameter $r_0 = 1.12\,\mathrm{fm}$. As compared to formula (6) and as shown in fig. 3, the option "Hauser-Feshbach", alternatively implemented in GEMINI for $Z \leq 2$ emission, results in very similar barriers for protons or alphas, respectively.

Figure 3 shows the Coulomb barriers experienced by protons and α-particles emitted from an excited compound nucleus with atomic number Z. In the limit of low excitations, the RAL and Dresner descriptions correspond within several per cent and are, in case of He, also in agreement with the barriers applied in GEMINI. However, the barriers reduce drastically if, in the case of the RAL option, higher excitation energies are regarded. Since the charged particles are confronted with a lower barrier, they could be released much easier and the originally deposited thermal energy is effectively cleared away not only by neutrons but also by charged particles. The energy spectra of charged particles (in particular the spectra of d, t, ^{3}He and ^{4}He particles) are clearly enhanced at low kinetic energies in disagreement with measured spectra [21]. Once the energy conservation must be fulfilled, the variation of the Coulomb barriers likewise has an influence not only on the kinetic energy spectra, but also on the multiplicities of the observed neutrons as will be discussed in more detail in sect. 6. The question raised —but not to be answered here— is whether a decrease of the Coulomb potential with increasing excitation energy is physically justified. On one hand, authors determine inverse reaction cross-sections according to formulas which take a decrease of the Coulomb potential with increasing excitation energy into consideration [59], on the other hand, people claim the Le Couteur approach to be responsible for overestimation of the helium production cross-sections in structural materials irradiated by protons and neutrons at energies up to 800 MeV [61].

4 Hadronic showers

The energy losses of high-energy particles (≥ 1 GeV) traveling through matter are mainly determined by the production of secondary particles and not due to electronic stopping which is dominating at lower bombarding energies. Thus, the main feature of the cascade is an initial increase of the particle intensity with depth and time. If the energy of the produced secondary particles is high enough, they in turn knock out additional particles. There exists however a physical limit for the development of further cascades, because the initial energy of the primary particle is distributed among the produced particles. Therefore, the multiplicities tend to decrease during the cascade process and fade away because the average energy of the cascade particles decreases and a greater fraction of the individual particle energy is now dissipated by ionization losses. At the end of the inter-nuclear cascade process, subsequent emission of many low-energy particles, mainly neutrons, takes place, known as evaporation process [51].

The complexity and entanglement of all intra- and inter-nuclear cascade processes, at the end causing the production of neutrons, requires a complex record keeping of all particles actually participating in terms of energy, direction and location. The simulated propagation of the three-dimensional hadronic showers following the bombardment of cylindrical lead targets of 35 cm × 15 cm (for the length and diameter, respectively) by 0.4, 1.2 and 2.5 GeV protons is illustrated in the contour plots of fig. 4.

In the HETC + MORSE Monte Carlo calculations to produce the data for fig. 4, the cylindrical target is divided into cylindrical zones of 0.5 cm in radial (r) and 1 cm (z) in longitudinal direction and the *track length flux* [34] is estimated. The symmetry axis of the cylinder is oriented in z-direction and pointing downstream the proton beam. The track length flux of neutrons (left) and protons (right) reflects the radial and longitudinal propagation of particles involved in the intra- and inter-nuclear cascades inside the target volume. The track length flux comprises both —cascade and evaporation particles. Primary beam protons are *not* included for the proton track length flux in fig. 4. Multiplying the proton beam current (protons per second) by the track length flux specified in fig. 4, the flux generally used in units of $(1/\mathrm{cm}^2\mathrm{s})$ is obtained.

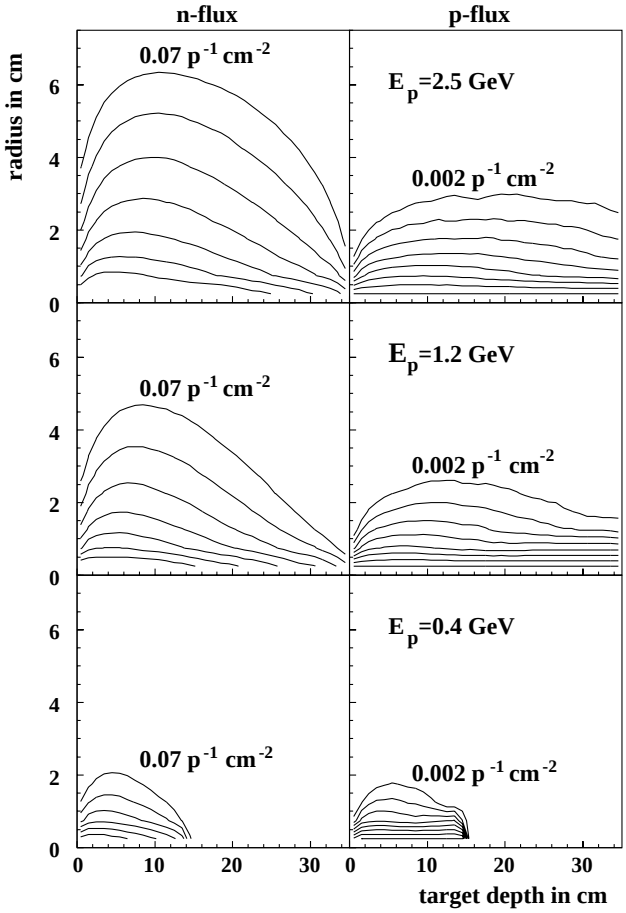

Fig. 4. Neutron and proton "track length flux" (per square centimeter and source proton, $\mathrm{cm}^{-2}p^{-1}$) of a hadronic shower in a cylindrical target of 35 cm × 15 cm lead as a function of incident energy of the protons. Lines are separated by factors of 1.5.

As a general trend, the higher the kinetic energy of the incident proton is, the deeper the penetration into the target. The spread in the radial direction is maximum after the hadronic cascade has propagated 5 to 10 cm in longitudinal direction. Neutrons tend to spread out radially much more than protons do, because especially low-energy protons experience high electronic stopping power and consequently short range. That is also why protons develop along their trajectory in a narrower cone. The absolute value of the track lenght flux estimator for neutrons is more than one order of magnitude larger than for protons, as seen in fig. 4.

For low incident proton energies (0.4 GeV) it is well shown that the cascade rapidly becomes extinct, since the leading particles are electronically stopped before being able to convert their energy effectively into the production of neutrons or protons. When the kinetic energy is large ($\approx$ GeV), the range due to electronic stopping power of protons for lead and mercury is greater than the length of the target. Although the presentation of hadronic cascades in the (r, z)-plane is illustrative to explain phenomenologically the interplay of intra- and inter-nuclear cascade descriptions and the well-known consequences of stopping powers applied to charged particles, a more quantitative analysis would include the study of kinetic energy and multiplicity spectra or angular distributions of particles released.

5 The NESSI experiment

As pointed out in the introduction, there is an application-driven demand for accurate experimental information regarding processes induced by energetic protons impinging on massive targets. Specifically, of great importance are neutron production cross-sections and neutron energy spectra for various incident proton energies, various target materials, and different target geometries. Clearly, such information is also of great value to nuclear science in general.

In the present study, strong emphasis is put on a comparison of model predictions with the data obtained with thick targets, where incident energetic protons give rise to cascades of nuclear reactions within the bulk target material. In these kinds of setups, charged reaction products are stopped within the target volume and only neutrons are detected. Furthermore results taken at thin-target measurements have been compared with corresponding simulations in order to decouple the primordial spallation reaction from the subsequent inter-nuclear cascade, thus imposing additional constraints for theoretical models [21, 22]. Both, thick- and thin-target experiments were carried out by the NESSI and PS208 collaboration. The respective setups are discussed briefly in following sections. A more detailed description can be found in references [10–12, 21–23, 62].

As mentioned previously, thin-target experiments are aimed essentially at studying the physics of intra-nuclear cascades, with reaction products having negligible chance for secondary interactions with the target matter. In the thin-target NESSI setup both, neutrons and charged reaction products are detected using two concentric 4π detector devices, the Berlin Neutron Ball (BNB) [14] and the Berlin Silicon Ball (BSiB) [21, 63]. In this setup, the target is placed in the common operational center of the BNB and BSiB. The latter detector is mounted inside the BNB reaction chamber.

5.1 The Berlin Neutron Ball (BNB)

The BNB [11, 14] is a spherical tank with an outer diameter of 140 cm and an active volume of 1500 liters, filled with gadolinium-loaded organic scintillator NE343. It contains a central reaction chamber of 40 cm diameter connected to a high-vacuum beam pipe. The active detector volume is viewed by 24 fast photomultipliers mounted on the outer shell of the BNB.

The operation of the BNB is based on the detection of gadolinium γ-rays from the capture of neutrons thermalized within the scintillator liquid. The thermalization of the reaction neutrons is a relatively fast process, occurring on a 0.1 μs time scale. It is accompanied by a light flash

generated mostly by the interaction of the recoiling nuclei (mostly hydrogen, but also carbon and oxygen) with the scintillator. This flash, combined with the light produced in the interaction of reaction γ-rays and charged reaction products with the scintillator, gives rise to a "prompt" signal [10,11] —one of the observables in NESSI experiments.

A prompt light flash indicates an energy deposit in the detector by any reaction product. As it is detected with virtually unit efficiency, it can be used to measure the total reaction cross-section, including reactions without neutron emission. Experimentally, one recognizes prompt signals based on their coincidence with valid "start" signals, which are generated by projectiles traversing a thin scintillation detector placed at the entrance to the BNB reaction chamber. The reaction probability P_{Reac} for thin targets is then obtained by comparing the number of prompt signals with the number of incident particles.

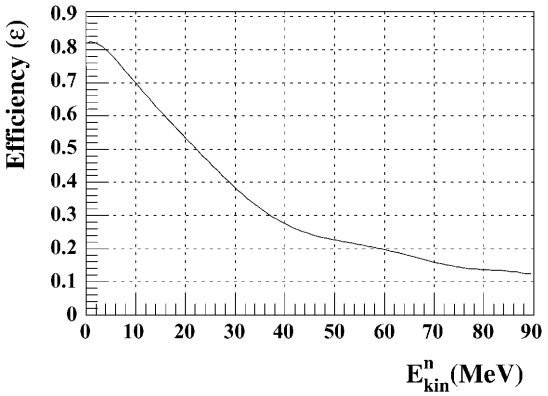

Fig. 5. Detection efficiency ε of the BNB as a function of neutron kinetic energy $\varepsilon(E^n_{\mathrm{kin}})$, as calculated with the DENIS code [64]. A parameterization of this curve is given in ref. [10].

5.2 The Berlin Neutron Ball efficiency

The above fast thermalization process is followed by a slow diffusion of the neutrons through the scintillator, before they are eventually captured by the gadolinium nuclei present in the scintillator. There is a statistically distributed time lapse for a thermalized neutron to "find" such a gadolinium nucleus and be captured, which occurs on a μs scale. The subsequent capture γ-ray cascade, with a total energy of approximately 8 MeV, produces a delayed light pulse. Due to the statistical nature of the thermalization and diffusion process, individual neutrons entering the detector volume at the same time instance, are captured at different times, spread over several tens of μs. It is this spread in capture times that allows one to count one-by-one the individual light pulses produced in different capture events and thus, (ideally) the number of neutrons that have entered the detector volume.

In applications of the BNB, neutron capture γ-rays are counted within a 45 μs counting gate following each reaction event. Hence, as a neutron multiplicity counter, the BNB is a slow device, prone to event pile-up in experiments with high beam intensity. It is also important to note that not all neutrons are thermalized within the active volume of the detector. Some, especially high-energy neutrons, escape this volume without being captured. Such neutrons are not counted, leading to an overall capture efficiency smaller than unity.

In the NESSI experiments, the BNB counts mostly low-energy evaporation neutrons, for which the detection efficiency is typically $\varepsilon \simeq 82\%$. In contrast, for pre-equilibrium and INC cascade neutrons of higher energy (30–50 MeV), the detection efficiency is of the order of 20–35%.

The theoretical neutron detection efficiency ε of the BNB as a function of neutron kinetic energy E^n_{kin} is shown in fig. 5. This efficiency was calculated using a Monte Carlo simulation code [64], assuming a light detection threshold of 2 MeVee (MeV electron equivalent[1]). In the simulation calculations, the latter threshold was matched to the experimental one, reproducing correctly the measured efficiency (82.6%) for 2.16 MeV fission neutrons emitted from a ^{252}Cf source.

In the NESSI experiments, the observed neutron multiplicities are averages over neutron energy spectra, weighted with the respective detection efficiencies. Since the information on kinetic energies of individual neutrons, E^n_{kin} is experimentally not available, the simulation calculations employ the neutron energy as calculated within the model. Additionally, the neutron detection efficiency is calibrated only at low neutron kinetic energies E^n_{kin}. At higher energies, the neutron detection efficiency is extrapolated, based on Monte Carlo calculations. It was checked by Y. Perier *et al.* [65] that such calculations reproduce satisfactorily the response of a similar detector for neutrons up to 70 MeV. As will be shown later in the upper panel of fig. 18 the bulk of neutrons are typically produced with energies lower than 10 MeV. Consequently, they are detected with high efficiency.

5.3 The Berlin Silicon Ball (BSiB)

In addition to the neutrons, in the thin-target experiments, charged reaction products were detected. Light Charged Particles (LCP: H and He isotopes), Intermediate Mass (IMF), and Fission Fragments (FF) were detected and identified by the Berlin Silicon Ball (BSiB) inside the BNB. The BSiB [21,63] is composed of 158 independent 500 μm thick silicon detectors approximating a 20 cm diameter sphere and covering a solid angle of about 90% of 4π. Due to absorption of LCPs in the target material, the overall detection efficiency for LCPs, calculated with Monte Carlo simulations [62], is about 79–84%, depending on the atomic number Z of the particle.

[1] The total reaction cross-section measured using the prompt response of the BNB with this threshold corresponds to an inelasticity of at least 2 MeV.

5.4 Trigger conditions

The setup for the measurement employing thick targets used only the BNB neutron detector. Massive targets up to 35 cm thick and 15 cm in diameter were used. Since essentially all the charged reaction products were stopped in the target block, only neutrons were detected (see also subsect. 5.6 below).

For targets thinner than 7 cm, a nuclear-reaction event was established based on the detection of a prompt light signal in coincidence with a valid start signal. For very thick targets (thickness $\geq$ 7 cm), on the other hand, the reaction event was signaled, and the data acquisition was triggered, just by a start signal from the in-beam scintillator, as shown by B. Lott *et al.* [13]. This procedure avoids bias in trigger due to the absorption of charged reaction products and γ-rays in the target material.

Since the height of the prompt signal originates from a variety of factors not exactly known (light conversion, reflection, absorption within the scintillator liquid etc.), a perfect analog is rather difficult to simulate. Therefore, in the simulation the trigger condition best resembling the experiment can be accomplished by setting a trigger to the excitation energy ($E^* > 0$) at the end of the INC process of the first spallation reaction. This indicates that an inelastic reaction has occurred. Another possibility is to trigger on any particle leaving the target, except the source particles leaving the target on its front side. Both Monte Carlo trigger conditions lead to exactly the same neutron multiplicity distributions.

5.5 Data correction

The neutron multiplicity distributions (M_nDs) measured with the above setup contained a random and target-frame-related background. The magnitude of the target frame background was determined in separate measurements made without target and subtracted from the measured "raw" multiplicities. The random background was measured on-line using a second, 45 μs long counting gate pulse, started 400 μs after the primary gate pulse. Subsequently, the experimental multiplicity distributions were corrected for this background by deconvolution techniques. All experimental neutron multiplicity distributions shown in the following [10] have also been corrected for the detector dead time of 35 ns and for multiple scattering, but *not* for the detection efficiency. The latter correction was included in simulation calculations in comparison with experimental data.

5.6 Additional neutrons produced in the scintillator liquid

In the experiment the targets are surrounded by a shell of scintillator liquid which acts as a moderator and at the same time as a reflector for neutrons. This enables neutrons (and other reaction products) originally produced in the target to be scattered into the liquid scintillator and potentially even causing interactions with the target when re-entering the target. In this section we study the contribution of additional neutrons being created by high-energetic baryons and mesons leaving the target and entering the scintillator liquid of the BNB. Those ones would experimentally give rise to an overestimation of the true number of neutrons coming from the target. As an approximation, the *leakage* spectra of different particles crossing the surface of the cylindrical targets towards the surrounding space have been calculated and these particles are considered as candidates for possible hadronic interactions or source of spallation reactions on C nuclei in the scintillator liquid.

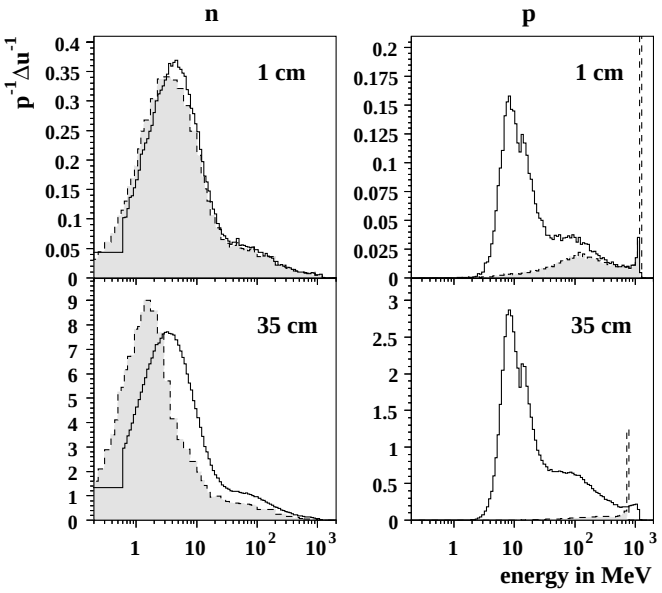

Fig. 6. Production (solid histogram) and leakage (dashed histogram) spectra of neutrons (left) and protons (right) for the reaction 1.2 GeV p + Pb. The dimension of the Pb target is 1 cm × 15 cm and 35 cm × 15 cm (length × diameter), respectively. The shaded area presents those particles actually entering the BNB. Simulated HERMES distributions are normalized per source proton and unit lethargy.

Figure 6 shows the yield (solid line) corresponding to all particles produced in the target block and leakage (dashed line) energy spectra not only for neutrons (left panels), as will be discussed in fig. 18, but also for protons (right panels). The spectra for 1.2 GeV proton-induced reactions on 1 and 35 cm Pb targets are confronted. While neutrons experience only a slight moderation when moving from the point of origin to the surface of the target, protons are drastically slowed down by electronic stopping. Only those protons having sufficient kinetic energy have a chance to leave the target surface and subsequently enter the scintillator liquid. The range of, *e.g.*, a 200 MeV proton in lead amounts to approximately only 5 cm and consequently the thicker the target the smaller the leakage spectrum, as demonstrated by the dashed lines for 1 and 35 cm in fig. 6. For the proton spectra, the peak found close to the beam energy (dashed line) reflects primary protons having lost all the more of their original incident

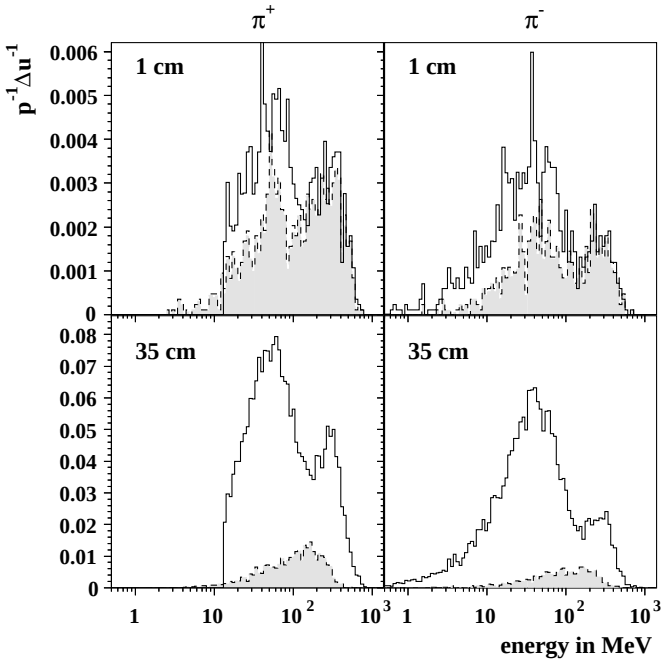

Fig. 7. Same as fig. 6 but for π^+ and π^-. Note the different absolute scales for the 1 cm and the 35 cm targets. Although the yield of pions is almost a factor of 10 higher in thick targets, the leakage finally is of the same order of magnitude.

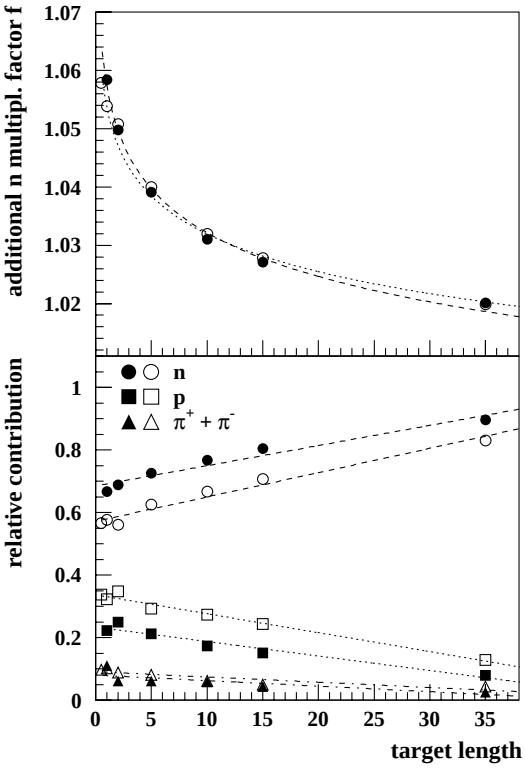

Fig. 8. Additionally produced neutrons by reactions of n, p and $\pi^{\pm}$ with the scintillator liquid for 1.2 GeV (open symbols) and 2.5 GeV (filled symbols) p + Pb as a function of target thickness. The diameter of the Pb target is 15 cm. The lower panel shows the relative contribution of n, p and $\pi^{\pm}$. Lines are to guide the eye. Calculations have been performed using the HERMES code system.

energy the thicker the target is. For the lower right panel of fig. 6 the peak at approximately 700 MeV is in agreement with the calculated energy loss of 1200 MeV protons impinging on the 35 cm Pb target. Finally the shaded grey area reflects the neutron and proton leakage including the geometrical acceptance of the BNB being slightly smaller than 4π essentially due to the conical openings for beam in/out. The lethargy $u = \ln(E_0/E_n)$ used in figs. 6 and 7 is the natural logarithm of the ratio of some fixed energy E_0 (*e.g.*, the incident energy) to the kinetic energy of the neutron E_n. Therefore a small kinetic energy corresponds to a large lethargy and a neutron kinetic energy equivalent to beam energy $E_n = E_0$ results in $u = 0$. Note that despite the logarithmic x-axis of the lethargy presentations, the integrals are a linear measure of the intensities.

Although the abundance of pions in absolute terms is much smaller than for protons or neutrons, the same phenomena are demonstrated in fig. 7 for π^+ and π^-. π^0 are not being transported in the codes, instead they decay spontaneously into two γ-rays. Regarding the dashed and the solid histograms of all panels in fig. 7 for both — π^+ and π^-— one observes a considerable reduction of the low-energy part of the leakage spectra as compared to the production spectra. High-energy pions are more likely to leave the target than the low-energy pions. In thick targets the pions are remarkably more attenuated when compared with thin targets. On the average also the kinetic energy of pions leaving the targets is decreasing with increasing target thickness. Consequently, the contribution of neutrons additionally produced in the scintillator liquid is expected to be largest for relatively thin targets —as will be shown in the following.

The percentage of neutrons and $\pi^{\pm}$ leaking the target that enters the BNB scintillator liquid is larger than 97.5% in the 1.2 GeV p + Pb cases (for both 1 cm and 35 cm targets). In the case of proton leakage the percentage entering the scintillator is only 24.6% and 32.4% for 1 cm and 35 cm, respectively. The relatively small ratio for p as compared to n or $\pi^{\pm}$ is due to the quite high probability for leading protons to leave the BNB through the 0° beam tube even for targets of 35 cm length. Also the energy loss in the BNB stainless-steel wall is slightly higher for protons as compared to pions.

The leakage spectra of n, p and $\pi^{\pm}$ shown in figs. 6 and 7 are the basis for rating the number of neutrons additionally produced in the scintillator liquid. As described in sect. 2 for HERMES generally the neutron spectrum is recomposed by the HETC ($E_{\rm kin} \geq 20$ MeV) and MORSE ($E_{\rm kin} < 20$ MeV). Here for reactions induced by spallation products in the scintillator liquid generating additional neutrons we consider only neutrons with kinetic energy larger than 20 MeV and charged particles (p, $\pi^{\pm}$) with $E_{\rm kin} \geq 1$ MeV.

As represented in the upper panel of fig. 8 the effect of creating additional neutrons decreases from 6% for thin targets to less than 2% for targets of 35 cm thickness relatively independent of the incident proton energy. The cal-

culation has been performed as a function of target thickness for a 1.2 GeV and 2.5 GeV p-induced reactions on Pb cylinders of 15 cm diameter. The decrease is partially due to the slowing down of charged particles in the thicker target, and in part to the considerably larger neutron production with a softer spectrum for the thicker targets. On the lower panel, the relative contribution of protons, neutrons and pions on the additional neutron production in the scintillator liquid is shown. Only those showers contribute to additional neutrons for which at least two neutrons are produced: $(n, xn...)$ with $x > 1$. For all target thicknesses predominantly the neutrons entering the liquid are producing additional neutrons. While their relative contribution is increasing with target thickness, the contribution from protons and pions is substantially decreasing due to self-screening effects in thick-target materials. Pions contribute only very little, because the abundance of pions created in the cylindrical targets is low. High-energy γ-rays from the π^0 decay have not been taken into account. For the higher incident energy a larger fraction of protons leaving the BNB via the exit cone is responsible for a lower relative contribution of protons.

In summary, the detector efficiency of the BNB as a function of kinetic energy is demonstrated to be well known. Since —as already mentioned— the information on kinetic energies of individual neutrons, $E^n_{\rm kin}$ is experimentally not available, a precise comparison between experiment and simulation can be performed on an event-by-event base only by taking the detector response into account in the calculations. In contrast all contributions giving rise to additional neutrons in the scintillator liquid are marginal and, despite quantified here, not included in the calculations. At most for thin targets maximal 6% of additional neutrons are created in the BNB.

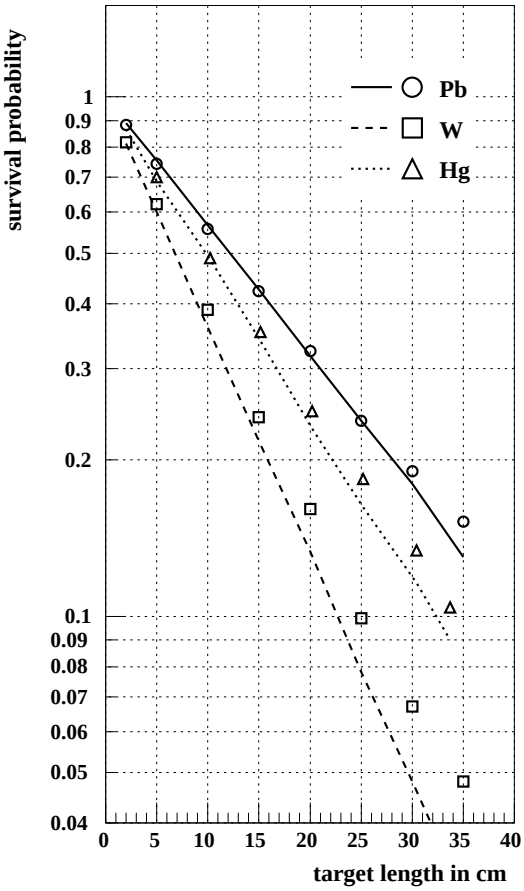

Fig. 9. Measured (symbols, [10]) and calculated survival probabilities $(1 - P_{\rm Reac})$ of the incident proton as a function of target length for 2.5 GeV p + Pb, Hg of 15 cm diameter and W cylinders of 8 cm diameter. Straight lines are HERMES calculations.

6 Comparisons model and experiment

In the present section, predictions by the models discussed above are compared to relevant experimental observations made in NESSI experiments. The study considers data on reaction probabilities $P_{\rm Reac}$, hadronic interaction length, average neutron multiplicities with reference either to the number of neutrons generated per reaction M_n or per incident proton M_n/p, and in particular neutron multiplicity distributions as obtained with 15 cm diameter Hg, Pb, and W targets bombarded with 1.2, 1.8, and 2.5 GeV protons. $P_{\rm Reac}$ is used to deduce the reaction cross-sections $\sigma_{\rm Reac} = -\ln(1 - P_{\rm Reac})A/(L\rho d)$ with A, ρ, d and L being the mass, density and thickness of the target and L the Avogadro number.

The two observables M_n/p and $P_{\rm Reac}$ are separately and independently measured in the NESSI experiment!

Due to the multitude of possible interlinkings of these models and the plurality of adjustable options and parameters within these codes here only a representative selection is executed.

6.1 Reaction cross-section and hadronic interaction length

Figure 9 illustrates the dependence of the proton survival probability $(1 - P_{\rm Reac})$ on target thickness. The data are for 2.5 GeV incident protons and for W, Hg, and Pb target cylinders of 15 cm diameter. As seen in this figure, the experimental data are well represented by HERMES calculations. The latter follow quite accurately the exponential law $1 - P_{\rm Reac} = \exp(-L/L_{\rm Reac})$, where L is the target length and $L_{\rm Reac}$ is the hadronic interaction length found to be 10.0, 14.1, and 17.9 cm, for W, Hg, and Pb targets, respectively. These hadronic interaction lengths resulting from the Monte Carlo calculations agree with published experimental values [10] of $10.84 \pm 0.2, 15.06 \pm 0.3$, and 18.00 ± 0.3 cm, respectively.

The experimental reaction cross-sections deduced from the measured $P_{\rm Reac}$, amount to $\sigma_{\rm Reac} = 1.46 \pm 0.03, 1.64 \pm 0.05$ and 1.69 ± 0.03 b for the three W, Hg and Pb targets, respectively. These values are slightly smaller than the results of the HERMES calculations of 1.62, 1.71 and 1.73 b for W, Hg and Pb, respectively.

An agreement of the same order of magnitude is found when the LCS2.70 and MCNPX codes were used instead of the HERMES code, demonstrating that the description of the observable σ_{Reac} poses no challenge to any of these codes. The above analysis is reflected also in tables 2 through 4 for different target thicknesses and the incident proton energies of 1.2, 1.8 and 2.5 GeV.

6.2 Neutron multiplicities

The term "neutron multiplicity" comprises all neutrons originating from primary and succeeding secondary reactions within the target material. As a matter of fact in the thick-target measurements only *neutron leakages* can be observed. The *neutron yield* is not accessible in any experiment since it reflects the neutron production at the point of origin when the neutrons are created, whereas the leakage spectrum can be measured as leaking neutrons from the target surface after they have been slowed down within the target material.

6.2.1 Mean neutron multiplicities

In fig. 10 M_n/p is plotted *vs.* the lengths of the lead, mercury, and tungsten target cylinders, respectively, and for the two incident energies of 1.2 and 2.5 GeV, as obtained in the NESSI experiments (open circles). As expected, for every target, the multiplicity increases with increasing target length, albeit in a non-linear fashion. Theoretical predictions (dashed lines) with the HETC + MORSE software package are compared in this figure to experimental data. Experiment and predictions include neutrons from both, the primary and secondary reactions. The calculations also account for the fact that neutrons are slowed down in the target material. Both, fission and elastic scattering were included. All other options have been chosen according to the standard set of parameters as summarized in table 1.

The solid curves in fig. 10 correspond to the predictions for the mean neutron (leakage) multiplicity per incident proton. In the case of the mercury target, the simulation calculations also account for the 1 mm thick walls of the stainless-steel capsules holding the liquid Hg.

As seen in fig. 10, the model calculations agree very well with the experimental observations, over a wide range of target geometries and target materials. The observed increase in the neutron multiplicity with increasing target length is due to an increase of the reaction probability, P_{Reac} and, to a lesser extent, to an increase of secondary reactions with the target length.

A more complete and systematic comparison of the experimental and model average neutron multiplicities $\langle M_n \rangle$ and reaction probabilities P_{Reac} is presented in tables 2 to 4 for different energies and target materials. For the sake of completeness, these tables include also the simulated neutron multiplicities, not corrected for the BNB neutron detection efficiency. These "true" multiplicities are denoted as $\langle M_n^c \rangle$. Numbers in parenthesis represent the

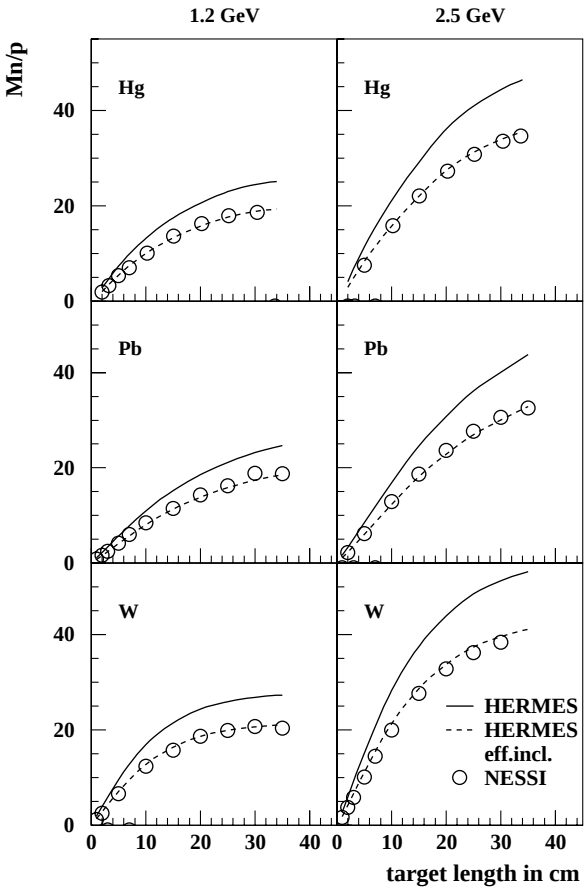

Fig. 10. Average neutron multiplicity produced per incident proton M_n/p as a function of target thickness (diameter 15 cm) for 1.2 and 2.5 GeV p + Hg, Pb and W. Solid line: HETC + MORSE, dashed line: HETC + MORSE with detector efficiency taken into account, ○: NESSI, experimental data from [10].

standard deviation of the distributions, respectively. The agreement between calculation and experiment for the second moment of the distributions within a few percent give additional confidence to the program packages under consideration. The statistical error of calculated mean values is typically of the order of 1%.

The comparison between theory and experiment will be separately discussed for Hg, Pb and W in the following.

6.2.2 Neutron multiplicitiy distributions

A typical, bell-shaped, experimental neutron multiplicity distribution is shown as open symbols in fig. 11. Here, P_{Reac} is plotted *vs.* the number of neutrons generated per reaction. When corrected for the finite neutron detection efficiency (cf. fig. 5), the results (dashed line) of the theoretical Monte Carlo simulation calculations (solid line) are seen to reproduce the data very well. Both, average position and shape of experimental and simulated distributions correspond well to each other. Note the specific strength of the NESSI experiment being able to provide

Table 2. Average neutron multiplicities $\langle M_n \rangle$ and reaction probabilities P_{Reac} for a cylindrical Hg target of 15 cm diameter bombarded with protons of various energies, E_p. $\langle M_n^c \rangle$ are mean neutron multiplicities before having taken detector efficiency into account. The dispersion of the M_nDs represented by the standard deviation is given in parenthesis. The standard parameter set was used for all calculations.

Length	HERMES			LCS2.70			MCNPX			Experiment	
	$\langle M_n \rangle$	$\langle M_n^c \rangle$	P_{Reac}	$\langle M_n \rangle$	$\langle M_n^c \rangle$	P_{Reac}	$\langle M_n \rangle$	$\langle M_n^c \rangle$	P_{Reac}	$\langle M_n \rangle$	P_{Reac}
					$E_p = 1.2\,\mathrm{GeV}$						
5 cm	17.2	23.0	0.313	18.0	24.2	0.310	18.1	24.2	0.315	16.9	0.313
	(10.0)	(13.0)		(10.6)	(13.6)		(10.6)	(13.6)		(9.6)	
15 cm	19.9	26.1	0.660	21.2	27.6	0.664	21.2	27.7	0.660	20.5	0.645
	(10.3)	(13.1)		(10.9)	(13.7)		(10.9)	(13.4)		(9.6)	
30 cm	21.2	27.5	0.889	22.4	29.0	0.875	22.5	29.1	0.885	21.9	0.847
	(9.8)	(12.2)		(10.3)	(12.9)		(10.3)	(12.9)		(9.6)	
					$E_p = 1.8\,\mathrm{GeV}$						
5 cm	21.9	29.5	0.315	23.4	31.5	0.311	22.0	29.9	0.313	21.7	0.296
	(13.0)	(17.2)		(14.0)	(18.3)		(13.2)	(17.3)		(12.0)	
15 cm	26.5	34.9	0.663	28.5	37.5	0.667	27.4	36.2	0.657	27.6	0.640
	(13.8)	(17.8)		(14.8)	(18.9)		(14.1)	(18.0)		(12.9)	
30 cm	29.6	38.6	0.886	31.9	41.4	0.874	30.6	40.0	0.887	30.6	0.851
	(12.9)	(16.4)		(13.9)	(17.6)		(13.2)	(16.7)		(12.0)	
					$E_p = 2.5\,\mathrm{GeV}$						
5 cm	26.1	35.5	0.314	28.5	38.6	0.310	27.1	36.8	0.310	25.1	0.301
	(16.0)	(21.5)		(17.6)	(23.4)		(16.7)	(22.1)		(14.5)	
15 cm	33.2	43.9	0.663	36.3	47.9	0.664	35.0	45.7	0.655	33.7	0.647
	(17.6)	(22.9)		(19.1)	(24.6)		(18.2)	(23.0)		(15.9)	
30 cm	38.5	50.3	0.887	41.5	54.2	0.874	40.1	51.6	0.884	38.4	0.866
	(16.5)	(21.1)		(18.0)	(22.0)		(17.1)	(21.2)		(15.0)	

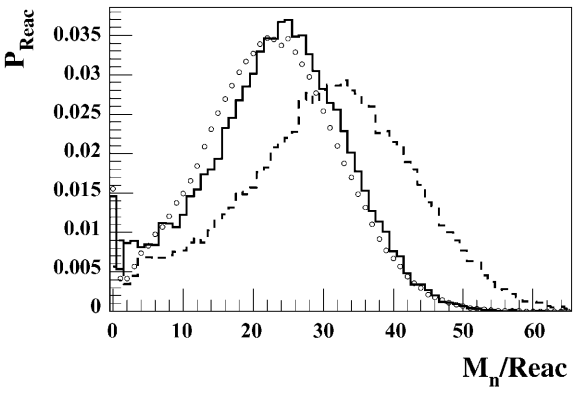

Fig. 11. Influence of the detector efficiency ε (cf. fig. 5) on the theoretical data obtained with GCCI (LCS) for a 35 cm long lead rod (diameter 15 cm) bombarded with 1.2 GeV protons. The dashed histogram represents MC data while the solid histogram shows efficiency folded data. The open symbols are the experimental data corrected for acquisition dead time and background, but not for efficiency.

even the probability to measure $M_n = 0$ neutrons in rather nice agreement with the simulated value. As can be seen from fig. 11, the finite detection efficiency of the BNB neutron detector has a significant effect on outcome of the measurements and needs to be accounted for in comparisons of theoretical calculations with experimental data. As, for example, for 1.2 GeV protons on Pb the calculations show that, *independent of the target thickness*, 80% of the total neutron leakage stem from the evaporation process. Especially for the remaining 20% of higher kinetic energy neutrons, the detection efficiency is low.

– Hg: As far as average values and Hg targets (table 2, fig. 10) is concerned, for all Monte Carlo codes considered here, one observes good agreement with the experimental results. Discrepancies between model calculations and experimental data are generally less than 5% for both, P_{Reac} and $\langle M_n \rangle$, and a broad range of energies. The maximum discrepancy is 7.4% in the case of the 5 cm Hg target bombarded with 2.5 GeV protons.

In figs. 12 and 13, experimental neutron multiplicity distributions induced by 1.2 and 2.5 GeV protons, respec-

Table 3. Same as table 2, but for Pb.

Length	HERMES			LCS2.70			MCNPX			Experiment	
	$\langle M_n \rangle$	$\langle M_n^c \rangle$	P_{Reac}	$\langle M_n \rangle$	$\langle M_n^c \rangle$	P_{Reac}	$\langle M_n \rangle$	$\langle M_n^c \rangle$	P_{Reac}	$\langle M_n \rangle$	P_{Reac}
					$E_p = 1.2\,\mathrm{GeV}$						
2 cm	14.6	20.3	0.107	15.1	21.0	0.107	15.2	21.0	0.106	14.5	0.113
	(8.5)	(11.5)		(8.5)	(11.1)		(8.7)	(11.7)		(8.6)	
15 cm	19.6	25.9	0.579	20.5	27.1	0.575	20.5	27.1	0.567	20.2	0.571
	(10.1)	(12.9)		(10.2)	(12.9)		(10.4)	(13.3)		(10.2)	
35 cm	21.4	27.9	0.867	22.2	29.0	0.863	22.1	28.8	0.859	22.2	0.848
	(9.7)	(12.2)		(9.8)	(12.3)		(10.0)	(12.6)		(9.9)	
					$E_p = 1.8\,\mathrm{GeV}$						
2 cm	18.0	25.3	0.109	18.9	26.5	0.107	18.7	26.3	0.107	17.7	0.113
	(10.8)	(14.9)		(10.7)	(14.2)		(11.1)	(15.3)		(10.4)	
15 cm	25.3	33.7	0.580	27.1	36.0	0.576	27.1	36.1	0.574	26.2	0.577
	(13.4)	(17.4)		(13.7)	(17.3)		(14.1)	(18.2)		(13.2)	
35 cm	29.2	38.4	0.869	31.2	40.9	0.864	31.4	41.2	0.861	30.5	0.853
	(12.8)	(16.3)		(13.0)	(16.2)		(13.4)	(17.1)		(12.7)	
					$E_p = 2.5\,\mathrm{GeV}$						
2 cm	21.3	30.3	0.108	22.3	31.7	0.107	22.3	31.8	0.107	19.4	0.117
	(12.9)	(18.3)		(13.0)	(17.2)		(13.6)	(19.2)		(12.3)	
15 cm	31.7	42.5	0.580	34.1	43.7	0.571	33.9	44.7	0.575	32.3	0.577
	(16.8)	(22.1)		(17.3)	(20.5)		(18.0)	(23.0)		(16.3)	
35 cm	37.7	49.7	0.865	40.5	50.5	0.860	40.4	52.2	0.861	38.4	0.848
	(16.3)	(21.0)		(16.6)	(19.0)		(17.2)	(21.3)		(15.6)	

tively in cylindrical mercury targets of various lengths are compared to the predictions of the codes HERMES and MCNPX.

As seen from these figures, the general shapes of the experimental distributions are well represented by simulation calculations using either of the codes, although somewhat better agreement is obtained with HERMES. However, there are systematic trends in quality of the agreement between calculations and data. In particular for the thin (2 or 5 cm) targets and the higher proton energy, theoretical calculations predict slightly higher average multiplicities than experimentally observed, as can be seen from the top panels of figs. 12 and 13, as well as from figs. 14 and 15 corresponding to Pb targets. Discrepancies seem to become larger for even higher energies [12]. The origin of these trends is presently not fully understood. The improved agreement between data and calculations for thick targets and low incident energies could conceivably be due to a cancellation of imperfections in the treatments of inter- and intra-nuclear cascades by the models. Since high neutron multiplicities are essentially due to evaporation, overestimation of the neutron multiplicities by the models may also be caused by an overestimate of the nuclear excitation energies as will be discussed in sect. 7 or too high Coulomb barriers (cf. subsect. 3.2) applied. The codes are also unable to reproduce the experimental data in the low-multiplicity region representing peripheral reactions. In this low M_n region both codes appear to overestimate the probabilities especially for the 2.5 GeV incident proton energy. On the one hand, the experimental precision for low neutron multiplicities is limited by threshold effects and accuracies in background corrections and, on the other hand, the description of the nuclear density profile of the nucleus has a large influence on the distributions for low M_n.

- Pb: Also for Pb targets the deviation of theoretical predictions with respect to experimental data decrease with increasing target thickness, while with increasing incident energy divergences increase. The maximum discrepancies are found for the 2 cm thick target bombarded with 2.5 GeV, namely 8.7 (8.3 %) for P_{Reac} and 13 (9.1 %) for $\langle M_n \rangle$ for LCS (HERMES). Note that the divergence for even higher incident proton energies (4.15 GeV) [12] still increase.
- W: Observations similar to those for mercury and lead were made for the tungsten target. At 1.2 GeV, agreement with experimental data is very good for the HERMES calculations, while it is still quite satisfactory for the LCS calculations (see fig. 16). However, for higher

Table 4. Same as table 2, but for W.

Length	HERMES			LCS 2.70			MCNPX			Experiment	
	$\langle M_n \rangle$	$\langle M_n^c \rangle$	P_{Reac}	$\langle M_n \rangle$	$\langle M_n^c \rangle$	P_{Reac}	$\langle M_n \rangle$	$\langle M_n^c \rangle$	P_{Reac}	$\langle M_n \rangle$	P_{Reac}
					$E_p = 1.2\,\mathrm{GeV}$						
2 cm	15.0	20.5	0.187	16.3	22.2	0.183	16.1	22.0	0.184	14.8	0.174
	(9.0)	(11.8)		(9.2)	(11.9)		(9.4)	(12.4)		(8.5)	
15 cm	20.9	26.9	0.784	22.6	29.0	0.780	22.5	28.9	0.781	21.6	0.729
	(10.2)	(12.7)		(10.6)	(13.1)		(10.6)	(13.2)		(10.2)	
35 cm	21.6	27.6	0.971	23.4	29.9	0.969	23.4	29.8	0.964	22.6	0.902
	(9.4)	(11.7)		(9.9)	(12.2)		(9.9)	(12.3)		(9.2)	
					$E_p = 1.8\,\mathrm{GeV}$						
2 cm	18.8	25.9	0.184	20.6	28.3	0.184	20.5	28.2	0.184	17.9	0.179
	(11.6)	(15.6)		(12.1)	(15.6)		(12.5)	(16.8)		(10.5)	
15 cm	28.5	36.9	0.786	31.5	40.5	0.780	31.5	40.7	0.786	28.9	0.747
	(13.8)	(17.4)		(14.5)	(17.8)		(14.7)	(18.5)		(12.9)	
35 cm	31.7	40.6	0.971	35.0	44.5	0.970	35.0	44.8	0.972	31.4	0.940
	(12.0)	(15.0)		(12.5)	(15.2)		(12.8)	(15.9)		(11.4)	
					$E_p = 2.5\,\mathrm{GeV}$						
2 cm	22.8	31.7	0.186	24.9	34.2	0.186	24.7	34.3	0.186	20.5	0.183
	(14.3)	(19.5)		(15.0)	(19.2)		(15.5)	(21.2)		(12.7)	
15 cm	36.7	47.6	0.782	40.6	48.4	0.780	40.7	52.7	0.781	36.6	0.758
	(17.9)	(22.8)		(18.7)	(21.0)		(19.4)	(24.7)		(16.5)	
35 cm	42.3	54.4	0.973	47.0	55.7	0.945	47.3	60.6	0.973	41.6	0.952
	(15.2)	(19.1)		(15.7)	(17.0)		(16.3)	(20.4)		(14.3)	

incident energies, the data clearly favor HERMES over LCS calculations. At 2.5 GeV, as seen in fig. 17, deviations of the LCS multiplicity distributions from the experimental data are quite substantial (17.6 % for a 2 cm long target).

In order to illustrate the differences between the HERMES and LCS predictions, the leakage and yield spectra of neutrons from the reaction p + W at 2.5 GeV are shown in the upper and lower panel of fig. 18, respectively. For example, the LCS and MCNPX neutron spectra in the lower panel of fig. 18 exhibit increased evaporative yields (between 1 and 5 MeV) and are slightly shifted to lower energies, as compared to HERMES calculations. This shift in neutron energy may be partly responsible for the differences in average and shape of the neutron multiplicity distributions predicted for the p + W reaction by the HERMES and LCS/MCNPX simulations, in conjunction with the RAL evaporation model (cf. table 4 and fig. 17).

The INC part of the spectra is very similar for all models. The small dip at approximately 7 MeV, seen in the LCS and MCNPX spectra displayed in the bottom panel of fig. 18, reflects the fixed 7 MeV cutoff energy for neutrons in the INC (cf. subsect. 6.2) calculations.

The most probable energy of neutrons leaked from the 35 cm × 15 cm (lenght × diameter) W target (upper panel in fig. 18) is approximately 0.6 MeV. This substantial decrease in energy, compared to the spectrum of neutrons at the moment of production seen in the bottom panel of this figure, is a result of the moderation of the neutrons within the target volume. The differences in the primary evaporative energy spectra predicted by the HERMES and LCS/MCNPX packages are seen to be largely washed out in the moderation process. Consequently, differences between the predictions by models for neutron production cross-sections (most apparent for W, cf. fig. 17) at high incident proton energies can probably not be traced back to differences in the treatment of the transport process. As seen in table 4 and fig. 17, for tungsten targets and all incident energies, the HERMES calculations achieve a better agreement with averages and shapes of the experimental neutron multiplicity distributions than LCS or MCNPX calculations do.

6.2.3 The GCCI level density and the MPM

In the case of the lead target bombarded by 1.2 GeV protons, a study of the sensitivity of the predictions to the

Table 5. $\langle M_n \rangle$ for a cylindrical lead rod of 15 cm diameter bombarded with 1.2 GeV protons. For LCS the GCCI and MPM + GCCI input parameters were used.

Length	LCS (GCCI)		LCS (MPM + GCCI)		Experiment
	$\langle M_n \rangle$	$\langle M_n^c \rangle$	$\langle M_n \rangle$	$\langle M_n^c \rangle$	$\langle M_n \rangle$
2 cm	16.0	22.1	14.9	20.8	14.5
5 cm	16.8	23.4	16.7	22.9	16.8
15 cm	21.2	28.0	19.7	26.4	20.2
35 cm	22.9	29.9	21.2	28.0	22.2

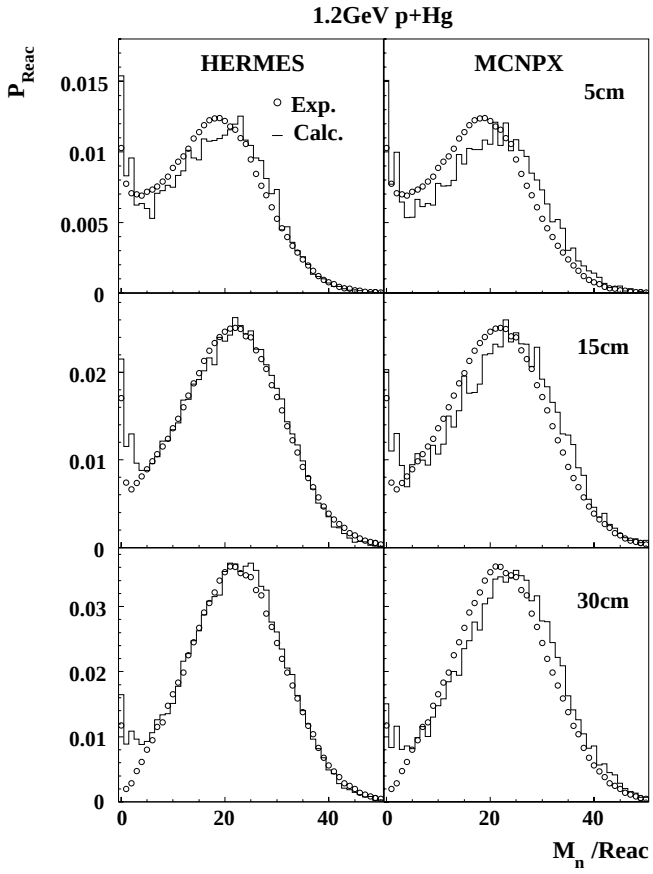

Fig. 12. Comparison of HERMES (left), MCNPX (right) and experimental data (○) for Hg targets of various lengths bombarded with 1.2 GeV protons. Experimental data from [10].

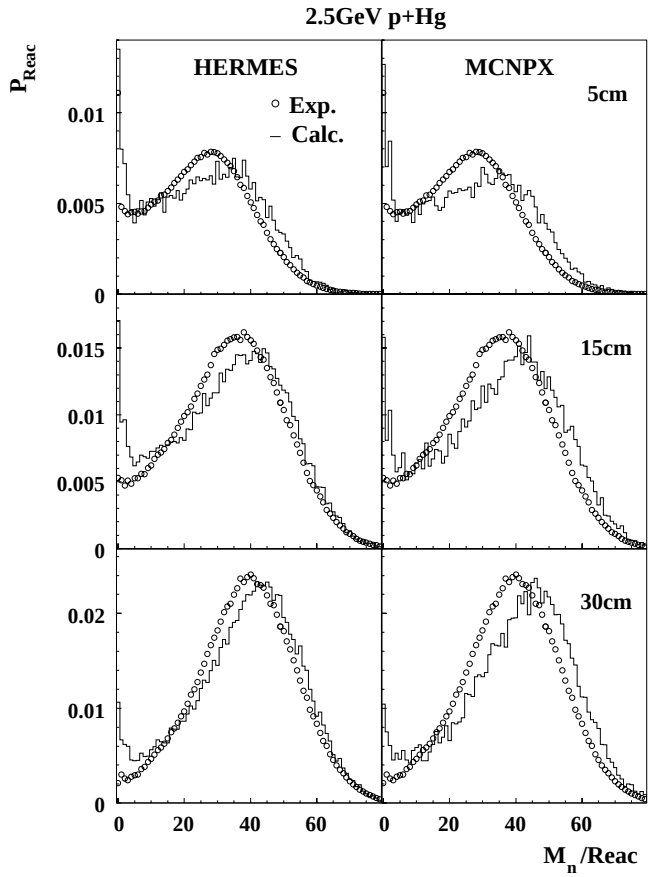

Fig. 13. Same as fig. 12, but for 2.5 GeV incident protons.

assumed Gilbert-Cameron-Cook-Ignatyuk (GCCI) level densities (see subsect. 3.1) and Multistage Pre-equilibrium Model (MPM) was performed. Average multiplicities, $\langle M_n \rangle$ obtained from these studies are depicted in table 5.

The LCS package, used in conjunction with the GCCI level density parameterization (GCCI in table 5) tends to overestimate mean multiplicities, compared to the experimental values. This could be a reflection of an excess of the excitation energy available for evaporation following the INC stage of the process. Such excess may result from the neglect of pre-equilibrium emission or from an underestimate of the system temperature, related to the parameterization of the level density. Indeed, when an intermediate pre-equilibrium stage is introduced (MPM + GCCI), following INC and preceding evaporation, neutron multiplicities are reduced on average by more than one unit. This is so, because particles from the pre-equilibrium stage have on average higher kinetic energies than thermal particles (see fig. 19) reducing thermal excitation energies and, hence, average multiplicities. In addition, the low-multiplicity events associated with peripheral reactions are somewhat better described, when the pre-equilibrium stage is included in the calculations (not shown here). In general, improved agreement between experimental data and theoretical predictions is achieved when the pre-equilibrium model is used together with the GCCI description. Note that in the LCS codes the recommended and default parameter setting is indeed the GCCI

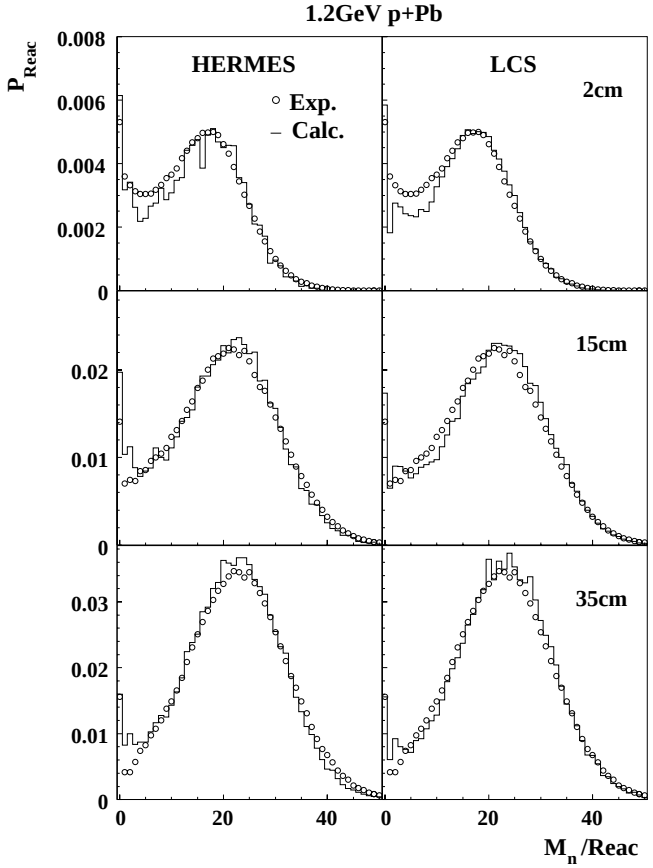

Fig. 14. Comparison of HERMES (left), LCS2.70 (right) and experimental data (○) for Pb targets of various lengths bombarded with 1.2 GeV protons.

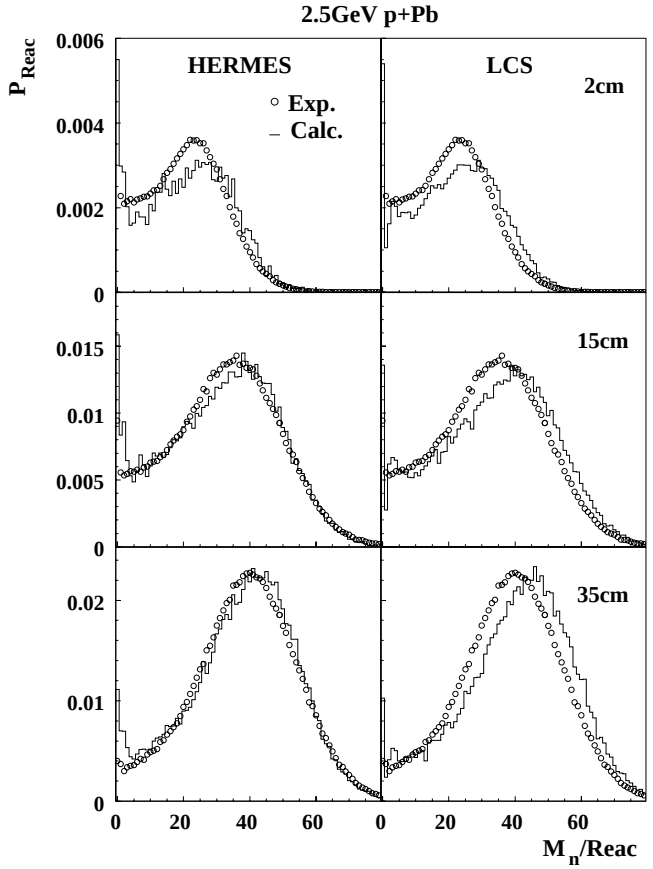

Fig. 15. Same as fig. 14, but for 2.5 GeV incident protons.

option and pre-equilibrium switched on, however to allow for a direct comparison of similar physics models in HERMES different options for LCS had been chosen in the current paper.

In summary, all three packages —HERMES, LCS, and MCNPX, provide an acceptable quantitative description of neutron production in cylindrical targets of various lengths, for proton energies up to 2.5 GeV. The agreement with the experimental data is generally within 10%. Only for the highest incident proton energy of 2.5 GeV and the dense tungsten target material, the predictions by the MCNPX and LCS codes deviate from the data by more than this margin (almost 18%). The model calculations show remarkable stability with respect to reasonable variations in the model parameters or assumptions. For example, varying the level density parameter B_0 within reasonable limits, or including pre-equilibrium neutron emission, may alter the neutron production only by approximately one neutron in the case of 1.2 GeV incident protons.

6.3 Influence of the Coulomb barriers on production cross-sections

By default LAHET and HERMES HETC exert the RAL fission/evaporation code [47,48] which on its part reduces the Coulomb barriers with increasing E^* as discussed in subsect. 3.2. The production cross-sections for H (all targets) and He isotopes (for heavy targets) are generally overestimated by a factor of approximately two for Bertini based codes (HERMES, LAHET using RAL evaporation/fission model), while the INCL2.0 code coupled to the statistical evaporation model GEMINI [60] gives reasonable agreement with the NESSI experimental data [21], as representatively demonstrated as a function of Z_{target} in fig. 20 for 1.2 GeV proton-induced reactions. While for the LAHET code system applying the ORNL fission/evaporation formalism (dash-dotted line in fig. 20) *not* scaling down the Coulomb barriers with E^*, the He production cross-sections reduce drastically below the experimental values, the predicted production cross-sections for H isotopes in contrast are still larger throughout all considered target nuclei. The fact of smaller He cross-sections predicted with the LAHET/ORNL fission/evaporation formalism is found to be a bit surprising, because for He isotopes not only the Coulomb barriers of GEMINI and LAHET/ORNL are similar (cf. fig. 3), but also the thermal excitation energies right after the INC used as input for GEMINI are smaller than for LAHET, as will be shown in fig. 22. This remarkable finding is interpreted [66] by

1. the Coulomb barriers (at $E^* = 0$) for protons being considerably smaller in LAHET than in GEMINI (cf. fig. 3) and

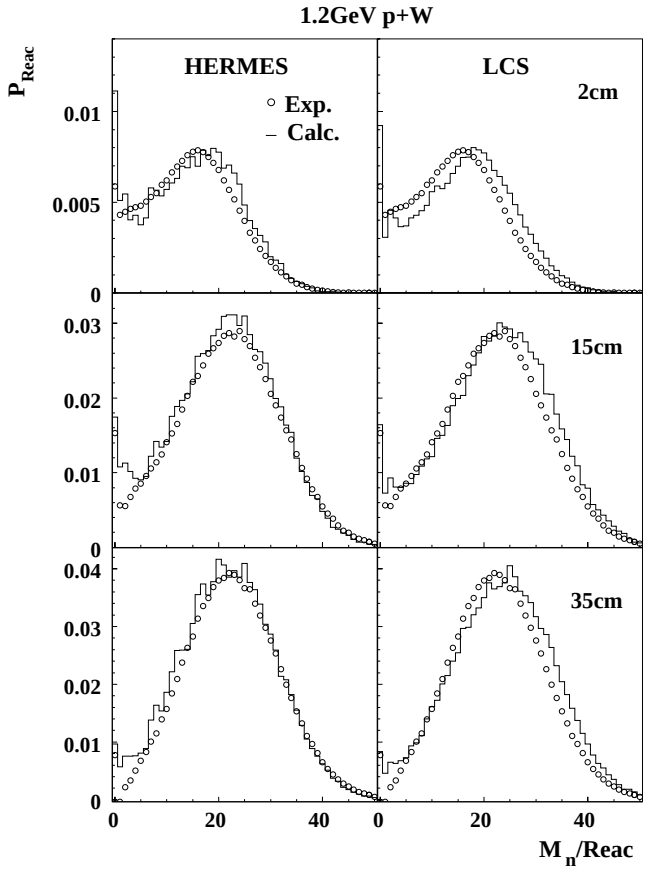

Fig. 16. Same as fig. 14, but for 1.2 GeV incident protons on W.

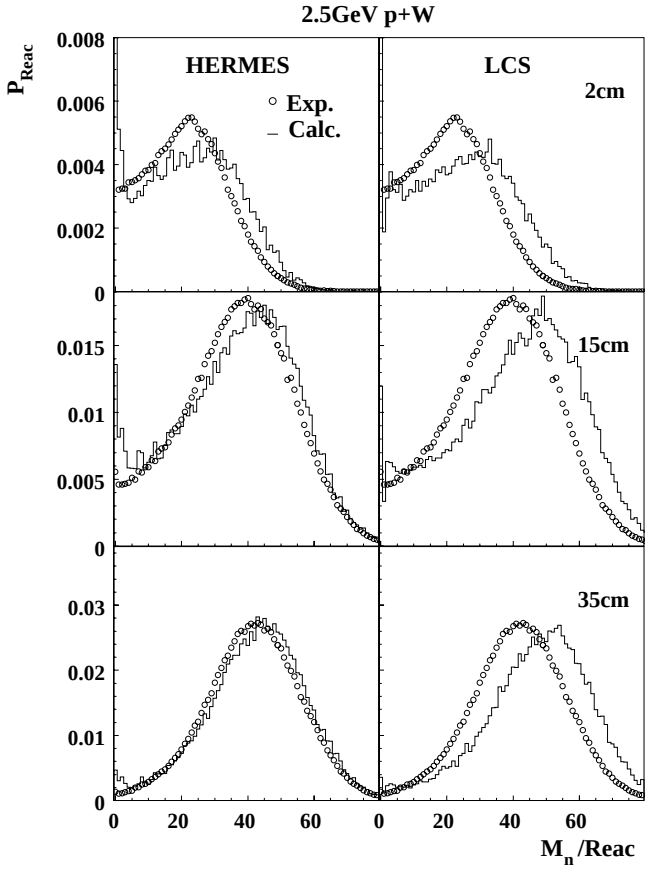

Fig. 17. Same as fig. 16, but for 2.5 GeV incident protons.

2. an increasing fraction of ^{5}He being produced in addition to stable ^{3,4}He isotopes in GEMINI.

Likewise —as discussed in subsect. 3.2— a considerable feedback on the neutron kinetic energy spectra and multiplicities is caused by the variation of the Coulomb barriers applied in the evaporation codes, because changing the emission width for charged particles effects at the same time the emission probability for neutrons, the two emissions being in competition.

For thick targets the influence of modifying the Coulomb barriers on the M_nDs is demonstrated in fig. 21 for 1.2 GeV proton-induced reactions on cylindrical lead rods of 15 cm diameter and 2 or 35 cm length, respectively. The calculations are performed with the Bertini-type INC implemented in MC4 [33]. Optionally, the Coulomb barriers could either be kept constant (dashed line) or reduced with E^* (solid line) as specified in fig. 3.

The corresponding mean neutron multiplicity decreases from $\langle M_n \rangle = 16$ (27) to 15 (25) for 2 cm (35 cm) length when reducing the Coulomb barrier with E^*, because at the expense of neutrons more charged particles are released. Note also that the average multiplicities following the MC4 calculation seem to be slightly higher than the HERMES values (cf. table 3 and fig. 14) for the same reaction. This phenomenon —specifically dominant for high values of M_n— is all the more pronounced as the target gets thicker and could be related to a different propagation of the hadronic shower within MC4. As compared to the experimental M_nDs the RAL description coincides better with the NESSI data having averages of $\langle M_n \rangle = 14.5$ (22.2) for 2 cm (35 cm), respectively. As expected, the integral reaction probabilities are not affected by the alteration of the barriers and amount (in agreement with the experiment) to 11 and 87% for 2 and 35 cm thick lead targets, respectively.

7 Deficiencies and particular variations within the codes

The previous sections documented a very good general agreement between experimental and calculated neutron multiplicities. If one decouples however the entire transport of the whole particle ensemble within thick targets and regards the primary reaction (one single nuclear reaction in thin targets) and specific decay channels (protons, neutrons, π,...) separately, then serious inconsistencies not only between experiment and simulation, but also among the codes themselves arise. This already indicates a kind of compensatory effect or redistribution of the total available energy in thick as compared to thin targets.

More specifically it is obvious, *e.g.*, that using Bertini-like intra-nuclear cascade codes we obtain thermal excita-

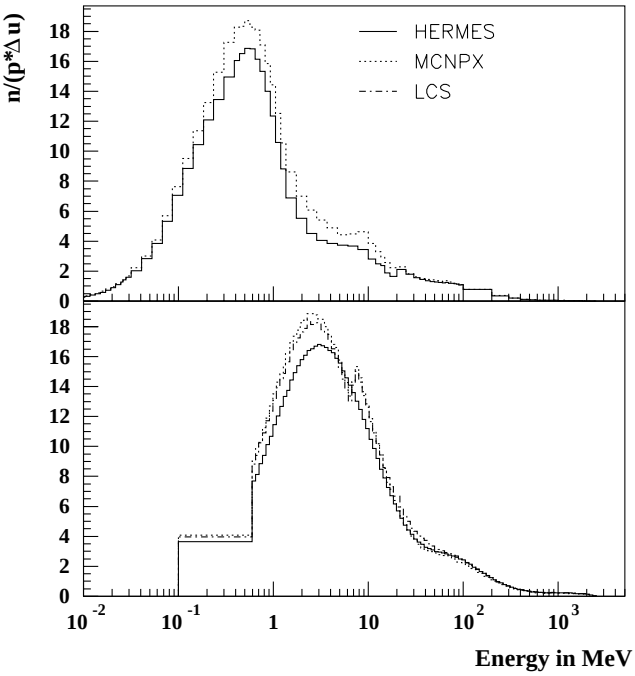

Fig. 18. Leakage (upper panel) and yield (lower panel) spectrum of neutrons for the reaction 2.5 GeV p + W using the standard parameter set. The dimension of the W target is 35 cm × 15 cm (length × diameter). The simulated HERMES, MCNPX and LCS distributions are normalized per source proton and unit lethargy.

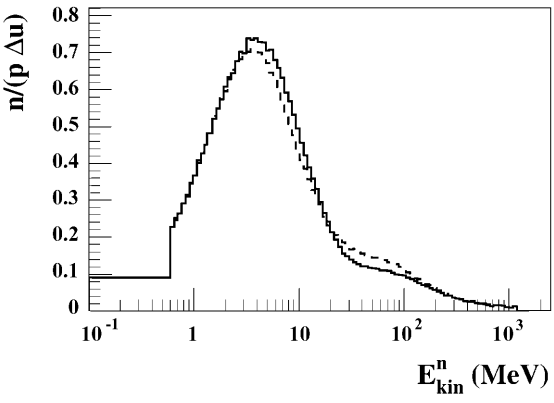

Fig. 19. Comparison of the theoretical neutron yield spectra resulting from the bombardment of a 2 cm long Pb target with 1.2 GeV protons. The dashed line represents the calculation with LCS using the pre-equilibrium and GCCI model (PREEQ + GCCI), while the solid line indicates the values obtained with the standard parameter set (cf. table 1). Curves have been normalized per unit lethargy Δu and source proton.

tion energy distributions in the residual nuclei after INC which are extending to larger values than the distributions of the INCL2.0 calculations do for the very same incident proton energy —as demonstrated in fig. 22.

For the cutoff conditions determining equilibration standard parameters have been taken (table 1). ISABEL and INCL2.0 calculations have been renormalized to the reaction cross-section of 1688 mb (p + Au) which is widely

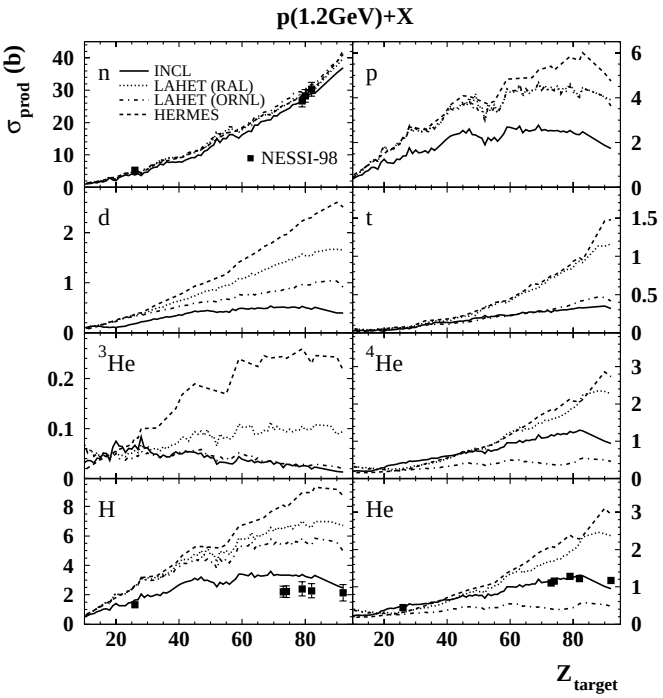

Fig. 20. Production cross-sections of neutrons, H and He isotopes as a function of the atomic number Z following the bombardment of 1.2 GeV protons. Various lines are representing LAHET/ORNL, LAHET/RAL, HERMES and INCL2.0 + GEMINI calculations, scriptsize■: NESSI data from [21,67]. The lower cutoff energy for charged particles is 2.2 MeV, the upper ones are 26, 49 and 76 MeV for p, d and tritons, respectively (also considered in the simulations).

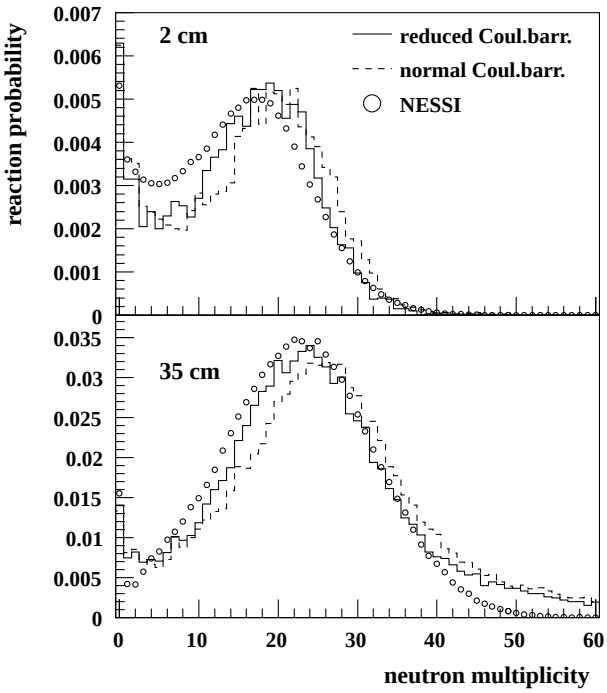

Fig. 21. Influence of the Coulomb barrier (cf. eqs. (3) and (4)) on the neutron multiplicity spectra for 1.2 GeV p + Pb. The calculations have been performed with the Bertini-type INC implemented in MC4 [33].

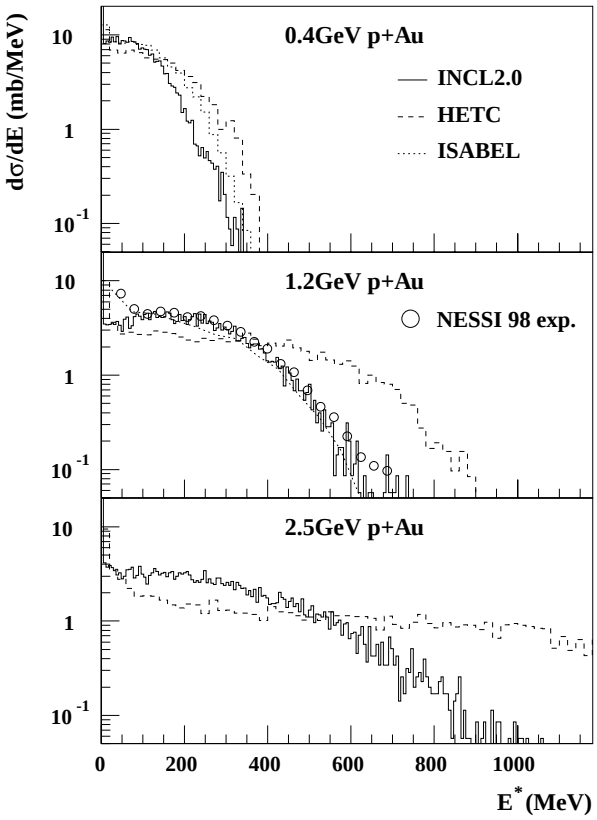

Fig. 22. Thermal excitation energy E^* differential cross-sections for 0.4, 1.2 and 2.5 GeV p + Au reaction following calculations with HETC (Bertini-like, dashed histogram) the INCL2.0 (Liege code, solid curve) and the ISABEL code (dash-dotted line). For 1.2 GeV deduced E^* distributions of the NESSI experiment (○) [21] are also plotted.

independent of incident proton kinetic energy. For thermal excitation energies larger than some 10 MeV and incident proton energies up to 1.2 GeV, the ISABEL code [45,46] coincides with the INCL2.0 predictions. For incident proton energies larger than 1.2 GeV, the validity range of ISABEL is exceeded [35] and consequently $\mathrm{d}\sigma/\mathrm{d}E^*$ distributions for 2.5 GeV are not shown in fig. 22.

The different cross-sections $\mathrm{d}\sigma/\mathrm{d}E^*$ at low E^* caused essentially by peripheral collisions can —among other things— be explained by differences in the nuclear density description of the nuclei. Probably the 16 step approximation of the nuclear density in the ISABEL code is responsible for the enhancement of $\mathrm{d}\sigma/\mathrm{d}E^*$ at low E^* as compared to the other models. For none of figs. 22, 23 and 24 the option pre-equilibrium has been applied.

When confronting $\mathrm{d}\sigma/\mathrm{d}E^*$ with experimental distributions [21], evaluated by applying a formalism described in [23], the INCL2.0 and ISABEL code coincides almost perfectly for both light (Fe) and heavy (Au) targets (fig. 22) while Bertini based codes overestimate $\mathrm{d}\sigma/\mathrm{d}E^*$ particularly for heavier targets. As, *e.g.*, compared to the 1.2 GeV p + Au experiment the average E^* is overrated by 110–140 MeV. ISABEL shows extremely nice agreement with experimental distributions even at low E^* for the reason just mentioned above.

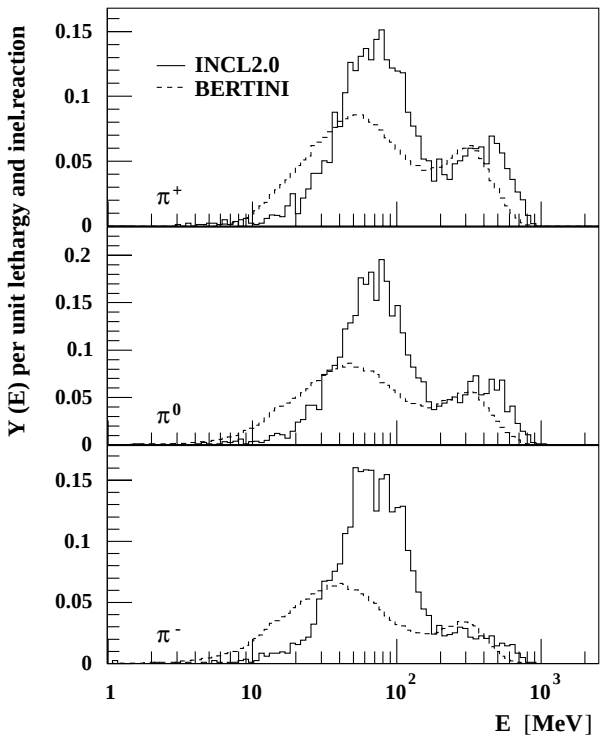

Fig. 23. Kinetic energy spectra of $\pi^{\pm}$ and π^0 per unit lethargy following an inelastic reaction of 1.2 GeV p on Au for INCL2.0 and HETC codes.

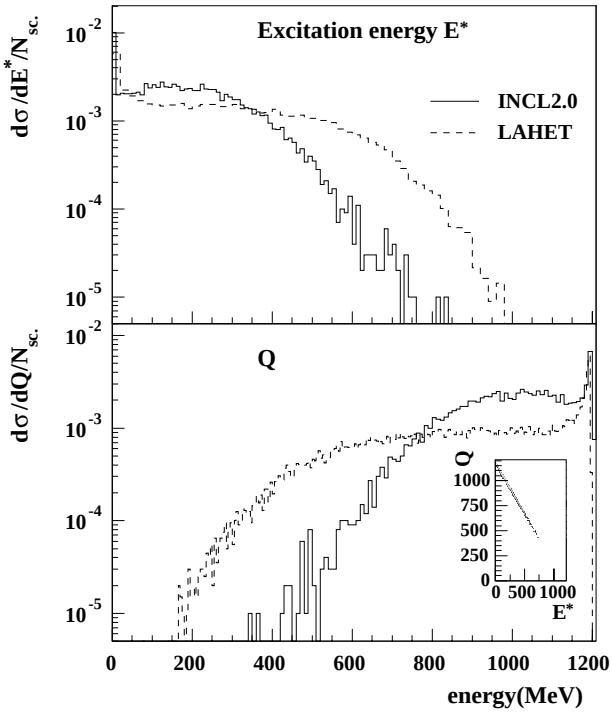

Fig. 24. The interplay between E^* and $\mathcal{Q}$ (cf. eq. (7)) during the INC is demonstrated for INCL2.0 in comparison with Bertini (LAHET) calculations for the 1.2 GeV proton-induced reaction on a thin Pb target. The inline graphic — demonstrating the energy conservation— shows the anticorrelation of E^* and $\mathcal{Q}$ crossing the axis intercept close to beam energy, respectively.

Table 6. Average kinetic energies $\langle E_{\rm kin}\rangle$ of pions (spectra shown in fig. 23), protons and neutrons and mean multiplicities $\langle M\rangle$ of $\pi^{\pm}, \pi^0, p$ and n produced during the INC for 0.4, 1.2 and 2.5 GeV p + Au. Also values for $\mathcal{Q}$ (cf. text and eq. (7)) and mean thermal excitation energies $\langle E^*\rangle$ are given.

Incident proton energy		0.4 GeV		1.2 GeV		2.5 GeV	
		$\langle M\rangle$	$\langle E_{\rm kin}\rangle$ (MeV)	$\langle M\rangle$	$\langle E_{\rm kin}\rangle$ (MeV)	$\langle M\rangle$	$\langle E_{\rm kin}\rangle$ (MeV)
INCL2.0	π^0	0.066	58.5	0.32	148.8	0.59	312
	π^+	0.067	57.7	0.28	158.7	0.47	325
	π^-	0.044	58.8	0.25	108.1	0.47	231
	proton	1.755	83.8	2.71	145.4	3.02	286
	neutron	3.535	39.0	4.70	76.2	4.96	146
$\mathcal{Q}$		320 MeV		993 MeV		2236	
E^* (MeV)		72		192		247	
Bertini	π^0	0.031	42	0.24	107	0.53	182
(LAHET)	π^+	0.021	47	0.22	133	0.48	220
	π^-	0.014	33	0.19	86	0.50	166
	proton	1.11	119.0	2.08	179.4	3.19	241
	neutron	2.34	53.0	5.05	67.5	8.38	80
$\mathcal{Q}$		267 MeV		873 MeV		1928 MeV	
E^* (MeV)		116		283		495	
ISABEL	π^0	0.014	56.8				
	π^+	0.009	73.3		not accessible		
	π^-	0.0047	51.1		due to limitations		
	proton	1.26	120.1		in the code		
	neutron	1.71	75.4				
$\mathcal{Q}$		286 MeV					
E^* (MeV)		100		173			

Average values of the E^* distributions summarized in table 6 indicate that only a small part (approximately 1/10 to 1/5 —depending on the nucleus, the incident energy, and the codes used) of the total available energy (incident kinetic energy of the proton) can be converted into thermal excitation energy. The remaining part is carried off by highly energetic nucleons and mesons during the fast INC. On the average, for large incident proton energies, the Bertini codes predict almost a factor of two higher E^*-values than INCL2.0 does.

The considerable deviation between Bertini, on one hand, and INCL2.0/ISABEL, on the other hand, for higher E^* is all the more pronounced as the energy of the incident proton increases. One assertion which could explain the disagreement is the way the originally transferred energy is being exhausted or carried away by the different exit particles. While the INCL2.0 code predicts many relatively highly energetic particles during the INC, the HETC codes (LAHET or HERMES) produce not only fewer, but also less energetic particles, as shown representatively in fig. 23 for $\pi^{\pm}$ and π^0 production following the reaction 1.2 GeV p + Au. All pion kinetic energy distributions shown in fig. 23 are based on the same inelastic reaction cross-sections of 1688 mb (for the reaction p + Au). Evidently the pion spectra show a shift of the π^+ energy distributions compared to the π^- distributions due to the repelling or attractive effects of the Coulomb field of the nucleus on the emitted pions. Since the pion model implemented in HERMES and LAHET is essentially the same, the kinetic energy spectra and pion multiplicities predicted by these codes coincide perfectly.

The appraisement of the quality of pion spectra and production cross-sections $\sigma_\pi^{\rm total}$ is almost impossible due to the lack of experimental data in the energy regime beyond 1 GeV. When comparing the INCL2.0 total π^+ and π^- production cross-sections (278 and 225 mb) with experimental results of Cochran et al. [68] for the reaction 730 MeV p + Pb ($\sigma_{\pi^+}^{\rm total} = 105\,{\rm mb}, \sigma_{\pi^-}^{\rm total} = 58\,{\rm mb}$) the Bertini approach ($\sigma_{\pi^+}^{\rm total} = 146\,{\rm mb}, \sigma_{\pi^-}^{\rm total} = 82\,{\rm mb}$) is found to overrate only slightly the experimental values. However the measured shape of the distributions [68] does not agree with the calculated one.

Conferring to table 6 as a matter of energy balance, the available thermal energy E^* right after the fast INC cascade is smallest for the INCL2.0 calculation since the energy carried off by fast cascade particles during the INC is generally larger than for Bertini-based models. For the

different codes, eq. (7) reflects the energy conservation fulfilled on an event-by-event base when considering the particle kinetic energies $E_{\rm kin}$ and the rest mass of 139.6 MeV for $\pi^{\pm}$ and 135 MeV for π^0 being abbreviated as $\mathcal{Q}$ in the following:

$$E_p = \underbrace{\sum_{\pi^0,\pi^{\pm},p,n} E_{\rm kin} + \sum_{\pi^0,\pi^{\pm}} m_{\pi} \cdot c^2}_{\mathcal{Q}} + E^* + S + E_{\rm rec}\,. \quad (7)$$

Adding up $\mathcal{Q}$, the thermal excitation energy E^*, the total sum of separation energies S and the recoil energy of the residual nucleus $E_{\rm rec}$ the incident proton energy E_p results. This proves the trivial fact that energy is conserved in all codes. Table 6 and fig. 24 oppose these quantities for the INCL2.0, Bertini and ISABEL, respectively. For the three codes the relative contributions of $\mathcal{Q}$, E^*, S and $E_{\rm rec}$ are different. As compared to the INCL2.0 approach for LAHET (Bertini INC) at the expense of larger E^* (upper panel in fig. 24) the sum of kinetic energies and multiplicities of emitted particles ($\mathcal{Q}$) is smaller, as shown in the lower panel of fig. 24. This is also shown in table 6 for the average values of $\mathcal{Q}$ and E^*. As far as the quantities defined in eq. (7) are concerned for incident proton energies up to 1.2 GeV, ISABEL results are similar to the predictions of INCL2.0. However, using the default depth of the nucleon potential of $V_0 = 40$ MeV and looking carefully at the energy balance the separation energy per nucleon being 1.5 MeV/nucleon in the INCL2.0 model seems unrealistically small as compared to 7 MeV/nucleon in the Bertini approach or literature. Therefore, the authors recommendation should be followed and V_0 should be put to 45 MeV resulting in the correct binding energies. However, this has very little influence on all observables printed in table 6.

All multiplicities given in table 6 refer to an inelastic reaction cross-section of 1688 mb —*not* to the number of primary source protons. The large particle transparency ($\approx 30\%$) in Bertini-like codes (using substantially larger nuclear radii) in relation to the INCL2.0 model ($\leq 3\%$) makes this exact specification and renormalization necessary.

As a consequence of the extremely high thermal excitation energy E^* in the Bertini-based codes (in addition to deficiencies in the evaporation codes) also the particle production cross-sections are overestimated. This applies especially to charged particles p, d, t, ^{3}He and α, because they are subject to the Coulomb barrier and therefore preferentially emitted from high excitation energies as shown representatively in fig. 20 in subsect. 6.3 for 1.2 GeV proton-induced reactions on a variety of target materials ranging from Fe to U.

A crucial aspect, however, directly biasing E^* after each intra-nuclear cascade are the cutoff criteria of the codes allowing for further decay of the equilibrated excited residual nucleus by means of sequential evaporation described by the statistical model. In the INCL2.0 code the equilibration time τ is determined by reaching a constant emission rate of cascade particles during the INC process. τ depends on the size of the nucleus, the impact parameter and on the kinetic energy of the incident proton. Typically τ is of the order of 10^{-22}s or 30 fm/c. The longer this somewhat "artificially" chosen time the smaller E^* being left for the evaporation process. In the Bertini-like codes the switching is performed when the most energetic scattered nucleon in the nucleus has decreased below a given cutoff energy of 7 MeV above the Fermi energy.

The question whether the different multiplicities and energies of particles are a matter of a different basic approach (following the cascade in time) or whether more sophisticated fundamental cross-sections in the INCL2.0 code —enabling a dissenting production mechanism— are responsible cannot yet be answered.

In summary, charged particle are, as compared to neutron production cross-sections, showing much more variations in literature both from the experimental point of view as well as from the calculational one. The NESSI experiment initiated some closer look to the widely used programs, but, in order to improve some of the identified model deficiencies, additional experimental data is required. In particular, detailed pion spectra of GeV induced spallation reactions are in dire need of.

8 Conclusion

The superior aim of the current contribution was to check, revise and improve the predictive power of nuclear reaction models for spallation source relevant data and the identification of deficiencies of existing INC/evaporation codes. The results of these findings can than be exploited to improve these codes. A multitude of nuclear model calculations has been performed and compared to latest benchmark experiments. The NESSI experiment at COSY Jülich has been consulted to validate models with regard to reaction cross-sections or reaction probabilities, neutron production cross-sections and multiplicity distributions following proton-induced reactions on thin and thick Hg, Pb and W targets in a broad range of incident energies. In the current contribution we outlined the influence of important parameters optionally chosen in the models, faced different approaches and confronted the model calculations with the NESSI data.

Due to the large variety of options, parameters, and —to some extent— liberties in the various models it is almost impossible to judge the quality of the codes in respect to all observables. Both the HERMES code system and the LCS or MCNPX packages master generally the prevision of neutron production in thick (and thin!) targets for a wide spectrum of incident energies and geometrical shapes of the target. All code packages convince of the bodacious describability of the complex circumstances regarding neutron production in thick targets. The predictive power of reaction probabilities and neutron multiplicities or neutron multiplicity distributions is almost perfect for the HERMES code for all target materials under consideration (Hg, Pb, W), but shows —especially for LCS and MCNPX— some weaknesses in the high incident energy domain (2.5 GeV) for dense targets like tungsten. HERMES coincides with the NESSI experiment within $\pm 4\%$

for average neutron multiplicities and therefore fulfills the grade of accuracy requested to design a target station for spallation neutron sources. Generally LCS and MCNPX overrate the neutron production by 4–8% as compared to HERMES calculations or the experiment. In LCS a part of these discrepancies can be eliminated by considering pre-equilibrium processes using the multistage exciton model. Currently HERMES appears to be best suited for predicting the neutron production in thick targets.

In the current calculations MCNPX version 2.1.5 has been applied. The Cascade Exciton Model (CEM) implemented in this version is not yet competitive. For example neutron production is significantly underpredicted and problems with low Z targets and high particle energies (≥ 1 GeV) are to be expected because the Fermi-breakup is not yet implemented into CEM. The comparisons performed here can usefully be repeated later when a future release of MCNPX will incorporate a more up-to-date version of CEM, which should show considerable improvement.

The complete implementation of a modern INC approach in MC4 is waiting for the latest release of the Liege (INCL3.0) code which is supposed to describe the excitation energy distributions and, as a consequence, the charged particle production cross-sections superior than the Bertini-based INC codes. This has already been indicated in the present contribution using the INCL2.0 version. It has also been demonstrated, that especially for large incident proton energies descripancies between the codes in pion production are obvious, most likely due to different absorption cross-sections of Δ resonances.

The reaction cross-sections predicted by all codes generally slightly exceed the experimental values. For Pb a minor deviation of 2% is observed while the discrepancy for W is at most 11%.

Finally we pinpointed some possible deficiencies of the models essentially related to presumably too high thermal excitation energies in the Bertini model. Also in the appended RAL fission/evaporation model Coulomb barriers are found to be underestimated. Even though in respect of such discrepancies the emission of charged particles in thin targets is drastically affected, the final abundance of neutron production in thick targets is accurately described.

The deficiencies are identified in the present contribution and shall be amended in future releases of high-energy transport codes. Although the state-of-the-art of computational models is sufficient in many cases for assessing spallation source/target systems performance, further "benchmarks" between users, experimentalists and code developers should be done in order to further improve the predictive power of nuclear reaction models.

The excellent proton beam of COSY and the help of the COSY team is very much appreciated. This research is partly supported by the TMR Program of the European Community under Contract No.: FMRX-CT98-0244, the German Helmholtz-Strategy Fonds and the French program GEDEON.

References

1. G.S. Bauer, *Proceedings of the 2nd International Conference on Accelerator-Driven Transmutation Technologies and Applications, Kalmar, Sweden, June 3-7, 1996*, edited by H. Conde, Vol. **II-II** (Uppsala University, Department of Neutron Research, 1996) p. 159, ISBN 91-506-1220-4.
2. *The European Spallation Source Study ESS*, Vol. **III**, *The ESS Technical Study*, Report ESS-96-53-M, ISBN 090 237 6659 (1996); `http://www.fz-juelich.de/ESS/`.
3. B. Appleton, Report PSI 95-02 Paul Scherrer Institut, *Proceedings ICANS-XIII*, edited by G.S. Bauer, R. Bercher (1995) p. 814, ISSN 1019-6447.
4. *Spallation Neutron Source SNS*, Status Report, Oak Ridge National Laboratory, USA; `http://www.ornl.gov/sns/`.
5. S. Nagamiya, *JAERI-KEK Joint Project on high Intensity Proton Accelerator, 9th International Conference on Radiation Shielding, International Congress Center, Tsukuba, Japan, October 17-22, 1999.*
6. H. Nifenecker *et al.*, *Hybrid Nuclear Reactors*, Institut des Sciences Nucleaire des Grenoble, ISN 99.04 (1999).
7. C. Rubbia *et al.*, *Conceptual design of a fast neutron operated high power energy amplifier*, preprint CERN/AT/95-44(ET) (1995).
8. J.C. Browne *et al.*, *Proceedings of the 2nd International Conference on Accelerator-Driven Transmutation Technologies and Applications, Kalmar, Sweden, June 3-7, 1996*, edited by H. Conde, Vol. **I-II** (Uppsala University, Department of Neutron Research, 1996) p. 101, ISBN 91-506-1220-4.
9. C. Bowman *et al.*, *Proceedings of the 2nd International Conference on Accelerator-Driven Transmutation Technologies and Applications, Kalmar, Sweden, June 3-7, 1996*, edited by H. Conde, Vol. **I-II** (Uppsala University, Department of Neutron Research, 1996) p. 11, ISBN 91-506-1220-4.
10. A. Letourneau *et al.*, Nucl. Instrum. Methods B **170**, 299 (2000).
11. D. Hilscher *et al.*, Nucl. Instrum. Methods A **414**, 100 (1998).
12. L. Pienkowski *et al.*, Phys. Rev. C **56**, 1909 (1997).
13. B. Lott *et al.*, Nucl. Instrum. Methods A **414**, 117 (1998).
14. J. Galin, U.Jahnke, Nucl. Part. Phys. **20**, 1105 (1994).
15. J.S. Fraser *et al.*, Phys. Can. **21**, 17 (1966).
16. T.W. Armstrong *et al.*, Nucl. Instrum. Methods **222**, 540 (1984).
17. R.G. Vassilkov *et al.*, KEK Report 90-25, *Proceedings ICANS-XI, KEK, Tsukuba, Japan, October 22-26, 1990* (National Laboratory for High Energy Physics, 1990) p. 340.
18. V.A. Nikolaev *et al.*, KEK Report 90-25, *Proceedings ICANS-XI, KEK, Tsukuba, Japan, October 22-26, 1990* (National Laboratory for High Energy Physics, 1990) p. 612.
19. M. Arai *et al.*, J. Neutron Res. **8**, 71 (1999).
20. D. Filges *et al.*, *Proceedings of the 2nd International Conference on Accelerator-Driven Transmutation Technologies and Applications, Kalmar, Sweden, June 3-7, 1996*, edited by H. Conde, Vol. **I-II** (Uppsala University, Department of Neutron Research, 1996) p. 490, ISBN 91-506-1220-4.
21. M. Enke *et al.*, Nucl. Phys. A **657**, 317 (1999).

22. C.M. Herbach *et al.*, *Proceedings of the 5th Workshop On Simulating Accelerator Radiation Environments (SARE-5), OECD-Headquarters, Paris, France, July 17-18, 2000*, ISSN 1433-559X, ESS 112-01-T.
23. F. Goldenbaum *et al.*, Phys. Rev. Lett. **77**, 1230 (1996).
24. T. von Egidy *et al.*, Eur. Phys. J. A **8**, 197 (2000).
25. X. Ledoux *et al.*, Phys. Rev. Lett. **82**, 4412 (1999).
26. Y.E. Titarenko *et al.*, *Proceedings of the 5th Workshop On Simulating Accelerator Radiation Environments, (SARE-5) OECD-Headquarters, Paris, France, July 17-18, 2000*, ISSN 1433-559X, ESS 112-01-T.
27. K. Ishibashi *et al.*, J. Nucl. Sci. Technol. **34**, 529 (1997).
28. S. Meigo *et al.*, Nucl. Instrum. Methods A **431**, 521 (1999).
29. W. Wlazlo *et al.*, Phys. Rev. Lett. **84**, 5736 (2000).
30. F. Rejmund *et al.*, Nucl. Phys. A **683**, 540 (2001).
31. T. Enqvist *et al.*, Nucl. Phys. A **686**, 481 (2001).
32. J. Benlliure *et al.*, Nucl. Phys A **683**, 513 (2001).
33. G. Sterzenbach *et al.*, *2nd International Topical Meeting on Nuclear Application of Accelerator Technology, AccApp98', September 20–23, Getlinburg, 1998*, ISBN 0-89448-633-0.
34. P. Cloth *et al.*, HERMES, Report Juel 2203, ISSN 0366-0885 (1988).
35. R.E. Prael *et al.*, Report LA-UR-89-3014 (1989).
36. H.G. Hughes *et al.*, MCNPX–The LAHET/MCNP Code Merger, X-Division Research Note XTM-RN(U)97-012, LA-UR-97-4891, Los Alamos National Laboratory (1997).
37. H.W. Bertini *et al.*, Phys. Rev. **134**, 1801 (1963).
38. J. Cugnon *et al.*, Nucl. Phys. A **470**, 558 (1987).
39. J. Cugnon *et al.*, Nucl. Phys. A **620**, 475 (1997).
40. R. Serber, Phys. Rev. **72**, 1114 (1947).
41. Ye.S. Golubeva *et al.*, Nucl. Phys. A **483**, 539 (1988).
42. M.B. Emmett, Report ORNL-4972 (1975).
43. W.R. Nelson *et al.*, SLAC-Report 265 (1985).
44. J.F. Briesmeister, Report LA-12625-M (1997).
45. Y. Yariv *et al.*, Phys. Rev. C **20**, 2227 (1979).
46. Y. Yariv *et al.*, Phys. Rev. C **24**, 448 (1981).
47. F. Atchison, Report Juel-Conf-34, Kernforschungsanlage Juelich GmbH (1980).
48. F. Atchison *et al.*, *Proceedings of a specialists' meeting: Intermediate Energy Nuclear Data: Models and Codes, May 30–Jun 1, Issy-les-Moulineaux, France* (AEN NEA, OECD-Documents, 1994) p. 349, ISBN 92-64-14278-9.
49. J. Barish *et al.*, Report ORNL/TM-7882, Oak Ridge National Laboratory (1981).
50. L. Dresner, Report ORNL/TM-196, Oak Ridge National Laboratory (1962).
51. V.F. Weisskopf *et al.*, Phys. Rev. **57**, 472 (1940).
52. D.J. Brenner *et al.*, *Proceedings of the 4th Symposium on Neutron Dosimetry, Neuherberg*, edited by G. Burger, H.G. Ebert, Vol. **II** (Commission of the European Communities, Luxembourg, 1981) EUR 7448, pp. 5-15.
53. R.E. Prael *et al.*, Report Los Alamos NM 87545 (1988).
54. R.E. Prael *et al.*, Report LA-UR-88-3238, Los Alamos National Laboratory (1988).
55. A.V. Ignatyuk *et al.*, Sov. J. Nucl. Phys. **21**, 256 (1975).
56. P.G. Young *et al.*, Report LA-12343-MS, Los Alamos National Laboratory (1992).
57. A. Gilbert *et al.*, Can. J. Phys. **43**, 1446 (1965).
58. O. Bersillon, Report CEA-N-2227, NEANDC (France) 220"L", INDC(E) 49/L (1981).
59. I. Dostrovsky *et al.*, Phys. Rev. **111**, 1659 (1958).
60. R.J. Charity *et al.*, Nucl. Phys. A **483**, 371 (1988).
61. A.Yu. Konobeyev *et al.*, *Data Library for Radiation Damage* (Carl Hanser Verlag, München, 1992) Kerntechnik 57, No. 3 (1992).
62. F. Goldenbaum, PhD thesis Berlin, unpublished (1996).
63. P. Figuera *et al.*, Z. Phys. A **352**, 315 (1995).
64. J. Poitou *et al.*, Nucl. Instrum. Methods **114**, 113 (1974).
65. Y. Perier *et al.*, Nucl. Instrum. Methods A **413**, 312 (1998).
66. D. Hilscher *et al.*, J. Nucl. Mat. **296**, 83 (2001).
67. D. Hilscher, private communication.
68. D.R.F. Cochran *et al.*, Phys. Rev. D **6**, 3085 (1972).